

VILNIUS UNIVERSITY
CENTER FOR PHYSICAL SCIENCES AND TECHNOLOGY

VYTAUTAS PURLYS

**THREE-DIMENSIONAL PHOTONIC CRYSTALS:
FABRICATION AND APPLICATIONS FOR CONTROL
OF CHROMATIC AND SPATIAL LIGHT PROPERTIES**

Summary of doctoral dissertation
Physical science, Physics (02P)

Vilnius 2015

The doctoral dissertation was prepared during 2010 – 2014 at Vilnius University.

Scientific supervisor:

prof. dr. Roaldas Gadonas (Vilnius University, Physical sciences, Physics – 02P).

Doctoral committee

- **Chairman** – prof. habil. dr. Vidmantas Gulbinas (Center for Physical Sciences and Technology, Physical sciences, Physics – 02P)

Members:

- dr. Gintaras Tamošauskas (Vilnius University, Physical sciences, Physics – 02P)
- doc. dr. Andrius Melninkaitis (Vilnius University, Physical sciences, Physics – 02P)
- dr. Gediminas Jonušauskas (University of Bordeaux, Physical sciences, Physics–02P)
- prof. habil. dr. Donatas Rimantas Vaišnoras (Lithuanian University of Educational Sciences, Physical sciences, Physics – 02P)

The dissertation will be defended under open consideration in the Council of Physics on the 13th of February, 2015, 14:00h at the Laser Research Center of Vilnius University, room 306, Saulėtekio 10, Vilnius, Lithuania.

The summary of the dissertation was distributed on the 13th of January, 2015.

The dissertation is available at Vilnius University, Center for Physical Sciences and Technology libraries, and VU website www.vu.lt/lt/naujienos/ivykiu-kalendorius.

VILNIAUS UNIVERSITETAS
FIZINIŲ IR TECHNOLOGIJOS MOKSLŲ CENTRAS

VYTAUTAS PURLYS

**TRIMAČIAI FOTONINIAI KRISTALAI: FORMAVIMAS
IR TAIKYMAS CHROMATINIŲ BEI ERDVINIŲ
ŠVIESOS SAVYBIŲ VALDYMUI**

Daktaro disertacija
Fiziniai mokslai, Fizika (02P)

Vilnius 2015

Disertacija rengta 2010 – 2014 metais Vilniaus universitete.

Mokslinis vadovas:

prof. dr. Roaldas Gadonas (Vilniaus universitetas, fiziniai mokslai, fizika – 02P).

Disertacija ginama Vilniaus universiteto fizikos mokslo krypties taryboje:

- **Pirmininkas** – prof. habil. dr. Vidmantas Gulbinas (Fizinių ir technologijos mokslų centras, fiziniai mokslai, fizika – 02P)

Nariai:

- dr. Gintaras Tamošauskas (Vilniaus universitetas, fiziniai mokslai, fizika – 02P)
- doc. dr. Andrius Melninkaitis (Vilniaus universitetas, fiziniai mokslai, fizika – 02P)
- dr. Gediminas Jonušauskas (Bordo universitetas, fiziniai mokslai, fizika – 02P)
- prof. habil. dr. Donatas Rimantas Vaišnoras (Lietuvos edukologijos universitetas, fiziniai mokslai, fizika – 02P)

Disertacija bus ginama viešame fizikos mokslo krypties tarybos posėdyje 2015 m. vasario 13 d. 14:00 val. Vilniaus universiteto lazerinių tyrimų centro 306 auditorijoje, Saulėtekio al. 10, Vilniuje, Lietuvoje.

Disertacijos santrauka išsiuntinėta 2015 m. sausio 13 d.

Disertaciją galima peržiūrėti Vilniaus universiteto, Fizinių ir technologijos mokslų centro bibliotekose ir VU interneto svetainėje adresu www.vu.lt/lt/naujienos/ivykiu-kalendorius.

Table of Contents

Abbreviations	6
Introduction	7
Object of the Thesis	9
Novelty	9
Practical novelty	10
Statements to defend	10
Approbation	11
Contributions	15
Structure of the Thesis	15
1 Introduction to photonic crystals	17
1.1 Temporal dispersion effects in photonic crystals	19
1.2 Spatial dispersion effects in photonic crystals	20
2 Principles of transparent materials laser fabrication	22
3 Experimental details of fabrication setups and materials	24
3.1 Three-dimensional microfabrication systems	24
4 Structural colors in woodpile photonic crystals	28
5 Beam focusing by woodpile photonic crystals	35
6 Control of spatial light spectrum by photonic crystals	40
6.1 Spatial filtering by chirped photonic crystals	43
6.2 Spatial filtering by axisymmetric photonic crystals	48
6.3 Supercollimation effect in axisymmetric photonic crystals	53
Reference list	58

Abbreviations

1D - one-dimension, one-dimensional
2D - two-dimension, two-dimensional
3D - three-dimension, three-dimensional
BZ - Brillouin zone
1BZ - First Brillouin zone
PBG - Photonic bandgap
PSG - Photonic stop (pseudo) bandgap
DLW - direct laser writing
MPP - multiphoton polymerization
SEM - scanning electron microscope
FDTD - Finite difference time domain
UV - ultraviolet
HeNe - Helium Neon (laser)
fcc - face centered cubic (lattice)
fct - face centered tetragonal (lattice)

Introduction

During the last year of my PhD studies I received thousands of questions what my thesis will be about. The first answer was always easy – "About the photonic crystals", however, the second question "What are the photonic crystals?" is never easy to answer, because it is too difficult to describe such an amazingly broad topic in just a few words. Perhaps the most common definition of PhCs defines them as microstructures, consisting of a periodically varying refractive index, which affects the motion of photons in much the same way that ionic lattices affect electrons in solids. A good example of such analogy is a frequency bandgap, which might occur in both PhCs and solids, and has the same origin. Frequency bandgap is a quality of crystals, which forbids the propagation of electrons or photons at certain or all directions. Bandgap present in solid crystals defines them as semiconductors or insulators, and in PhCs – as the optical insulators, i.e. mirrors.

Long before the invention of PhCs it was known that properly chosen multilayer structures may act as highly reflective mirrors due to constructive interference. Such mirrors might possess 99.999% or even larger reflection coefficient. In comparison, silver mirrors reflects only 95 – 99%, household mirrors – 88 – 92%. Almost perfectly reflective dielectric mirrors, often referred as Bragg mirrors, were described by Lord Rayleigh already in 1887 [1, 2] and are now classified as one-dimensional PhCs.

It took exactly one hundred years in order to understand that such highly reflective mirrors could be extended to two-dimensional or even three-dimensional cases [3, 4]. Originally, such periodic refractive index structures, called the photonic crystals, were thought to be useful for suppressing the spontaneous emission of surrounded particles, but soon it was discovered that, in addition to the frequency bandgaps, they can possess plenty other interesting features. In particular, temporal (chromatic) and spatial dispersion properties can be engineered by carefully selecting the geometry and refractive index of PhCs. This allows the control of light propagation in various ways. For instance, it is possible to form such PhCs, which allow the propagation of light without any diffraction for unlimited distances, independently on the angle of incidence [5–10]. Selecting other PhC parameters might lead to a negative refraction effect [11], when the light is refracted in the opposite direction

than usual. This effect allows to create a flat lens without optical axis, with far better resolution [12, 13]. Photonic crystals can also clean the spatial spectrum of the light beams [14, 15]. Such filters, which has a length of only ~ 1 mm, in future might replace conventional bulky spatial filtering setups, consisting of lenses and diaphragm. Also, PhCs might possess a slow light phenomenon [16], which could slow down the effective propagation of the light so, that the light could be outrun on foot. And that's not all the possible phenomena.

One-dimensional photonic crystals have been widely applied in practice. Such multilayer structures are generally used as reflection or anti-reflection coatings. Such coatings are broadly used in everyday devices, including mobile phones, cameras, laser printers, eyeglasses, binoculars, computer screens, etc. Two-dimensional PhCs are used in PhC hollow fibers, where the light is trapped at the core due to the bandgap of surrounded regions and not due to the total internal reflection as in the conventional fibers [17]. Three-dimensional PhCs are the most complex and currently not used because of the lack of fabrication technologies, but are under intense investigation. It is interesting that 3D PhCs, as well as 1D and 2D, are widely used or observed in nature for millions of years already. Various stones, plants, bugs, birds, fishes, and other creatures often possess natural PhCs, which are responsible for their bright vivid colors, improves the visibility in the dark or provides other, sometimes extraneous features. For example, it was observed that the PhCs in *Morpho* butterfly wings not only provide a bright blue color, but can also act as a high-speed bolometers, capable to sense infrared radiation via visible range spectral changes [18]. Numerous examples of natural three-dimensional photonic crystals does not leave any doubt that they will find their applications in practice.

The typical periods of PhCs are of the order of wavelength. The PhCs operating in the visible range are therefore difficult to fabricate, especially 2D and 3D. 1D PhCs are usually formed by evaporation techniques, while UV or electron-beam lithography techniques are used to form 2D PhCs. 3D PhCs are the most difficult to fabricate and there is no established techniques yet.

Paradoxically, the first experimental demonstration of working PhC was of the most complex – three-dimensional geometry [19]. It was designed to operate at microwave range, and was fabricated by mechanically drilling the holes in some precise directions. However, in order to produce PhCs operating in optical range, one needs to look for a higher-resolution material processing technologies, as well as appropriate refractive index materials. The first three-dimensional PhCs, working in optical range, were demonstrated in 1998 [20]. They had a bandgap at 10 – 14,5 μm range.

The crystals were made of silicon using UV lithography, commonly used in microelectronics. Even more effort has to be made in order to shift the operating range to the visible. One of the most promising technologies enabling the fabrication of high-resolution three-dimensional microstructures are the direct laser writing technologies, where a tightly focused femtosecond laser beam induces a permanent change in various glasses or photopolymers. By inducing such modifications point-by-point one can "draw" almost any three-dimensional shape microstructures having the refractive index contrast of approximately $\Delta n_{max} \approx 0.5$ in photopolymers and $\Delta n_{max} \approx 0.01$ in glasses. These technologies were first demonstrated in 1996–1997 and, due to their versatility and high resolution, still remain among the most attractive technologies in PhC research. On the other hand, even these high-resolution technologies are rarely sufficient to form required so small periods of the PhCs. This, therefore, leaves two alternatives: either to search for the ways to enhance the technologies, or to investigate how to achieve desired effects in PhCs with longer periods. The latter approach is common to all the PhCs described in this Thesis and also publications [A1-A8].

Object of the Thesis

By using the numerical calculation and direct laser writing techniques to fabricate and to characterize the photonic crystals, exhibiting structural colors, light focusing, and spatial filtering in the visible range effects.

Novelty

1. The structural colors, produced in three-dimensional polymeric woodpile photonic crystals with face centered cubic lattice geometry and relatively large lattice periods (approximately between 600 and 1000 nm), were demonstrated.
2. Flat lensing by three-dimensional photonic crystals was experimentally demonstrated in the visible range.
3. It was experimentally demonstrated that linear modulation of longitudinal periods (chirp) increases the filtering angular range in the photonic crystals for spatial light filtering.
4. The axisymmetric geometry of photonic crystals was demonstrated. It was shown, that in photonic crystals of this geometry the phenomena of spatial light filtering and far-field super-collimation occurs.

Practical novelty

In this Thesis various phenomena of light propagation are demonstrated experimentally in PhCs which have relatively large periods (about 2-5 times larger than conventionally expected). The larger periods enable an easier fabrication of PhCs by using existing technologies. All the PhCs investigated in this Thesis were fabricated by direct laser writing techniques. These techniques are based on the highly localized changes of the bulk of the transparent materials due to tightly focused ultrashort pulse laser beam. Such direct laser writing setups were constructed during the PhD studies as well as their automation software was created.

PhCs for structural color generation, flat lensing, spatial filtering and super-collimation were investigated. It is likely that such PhCs might be utilized in the future in various applications. For instance, PhCs for generation of structural colors might be attractive for sensing applications because of large surface area, for counterfeiting prevention because of complicated structure and for new generation displays because of bright non-bleaching colors. Flat PhCs lenses might be applied in various compact and sensitive devices, as they are flat and do not have optical axis, therefore are less sensitive to positioning. PhCs for spatial light filtering might replace conventional filtering techniques, consisting of two lenses and a diaphragm, as they are much more compact, mechanically stable and because of larger aperture might be used in high power applications. The demonstrated positive influence of longitudinal period linear chirp allows to broaden the filtered-out areas, therefore such chirped PhCs are the most potential candidates for spatial filtering applications. Demonstrated axisymmetric geometry of PhCs might be useful for uniform spatial filtering in all directions, this property is important in maximizing the quality of the light beams. The super-collimation effect, observed at the far-field, transfers the energy from periphery components to the center components and leads to well collimated beams. This effect might be useful for increasing the beam quality with smaller energy losses compared to other filtering techniques. All the discussed effects might be used in various micro devices as well as all-optical processors or lab-on-chips.

Statements to defend

1. Polymeric woodpile photonic crystals with face centered cubic lattice and transversal periods $\approx 600 - 1000$ nm, refractive index $\approx 1,5$ and linewidths $\approx 100 - 200$ nm exhibit structural colors.
2. At the presence of anomalously curved isofrequency countours of the higher order

photonic bands a flat lensing of visible spectral range light beams occurs in the polymeric woodpile photonic crystals.

3. Photonic crystal spatial filters with linearly varying longitudinal period enable several times broader angular filtering range.
4. Spatial light filtering phenomenon is observed in low refractive index contrast ($\Delta n \sim 10^{-3} - 10^{-2}$) axisymmetric photonic crystals, consisting of the layers of periodically varying diameter concentric rings, where each layer has opposite refractive index modulation distribution.
5. Super-collimation phenomenon, where the axial field components are enhanced several times by depleting higher angular components, might be observed in axisymmetric photonic crystals with small filtering angles and around twice longer length than required for spatial filters of the same geometry. This effect is not observed in two-dimensional photonic crystals of analogous geometry.

Approbation

A list of publications, which are included to the database of *Thomson Reuters Web of Science*, is provided here. In total there are 35 publications, 21 of these were published in journals having ISI impact factor. 8 publications are related to the Thesis.

Related publications:

- [A1] V. Purlys, L. Maigyte, D. Gailevicius, M. Peckus, M. Malinauskas, and K. Staliunas, Spatial filtering by chirped photonic crystals, *Phys. Rev. A* **87**(3), 033805 (2013)
- [A2] L. Maigyte, V. Purlys, J. Trull, M. Peckus, C. Cojocar, D. Gailevicius, M. Malinauskas, and K. Staliunas, Flat lensing in the visible frequency range by woodpile photonic crystals, *Opt. Lett.* **38**(14), 2376–2378 (2013)
- [A3] L. Maigyte, C. Cojocar, V. Purlys, J. Trull, D. Gailevicius, M. Peckus, M. Malinauskas, and K. Staliunas, Focusing by a Flat Woodpile 3D Photonic Crystal, 15th International Conference on Transparent Optical Networks (ICTON), 1-4 (2013)
- [A4] V. Purlys, L. Maigyte, D. Gailevicius, M. Peckus, M. Malinauskas, R. Gadonas, and K. Staliunas, Spatial filtering by axisymmetric photonic microstructures, *Opt. Lett.* **39**(4), 929–932 (2014)

-
- [A5] V. Purlys, L. Maigyte, D. Gailevicius, M. Peckus, R. Gadonas, and K. Staliunas, Super-collimation by axisymmetric photonic crystals, *Appl. Phys. Lett.* **104**(22), 221108 (2014)
- [A6] V. Mizeikis, V. Purlys, R. Buividas, and S. Juodkazis, Realization of Structural Color by Direct Laser Write Technique in Photoresist, *J. Laser Micro Nanoen.* **9**(1), 42 (2014)
- [A7] D. Gailevicius, V. Purlys, L. Maigyte, M. Peckus, K. Staliunas, Chirped axisymmetric photonic microstructures for spatial filtering, *J. Nanophoton.* **8**(1), 084094 (2014)
- [A8] V. Mizeikis, V. Purlys, R. Buividas, and S. Juodkazis, Structural colour of porous dielectrics processed by direct laser write technique, *Proc. SPIE* **8974**, 89740N (2014)

Other publications:

- [A9] M. Malinauskas, H. Gilbergs, V. Purlys, A. Zukauskas, M. Rutkauskas, and R. Gadonas, Femtosecond laser-induced two-photon photopolymerization for structuring of micro-optical and photonic devices, *Proc. SPIE* **7366**, 736622 (2009)
- [A10] M. Malinauskas, V. Purlys, M. Rutkauskas, and R. Gadonas, Two-photon polymerization for fabrication of three-dimensional micro- and nanostructures over a large area, *Proc. SPIE* **7204**, 72040C (2009)
- [A11] M. Malinauskas, H. Gilbergs, A. Zukauskas, K. Belazaras, V. Purlys, M. Rutkauskas, G. Bickaускаite, A. Momot, D. Paipulas, R. Gadonas, S. Juodkazis, and A. Piskarskas, Femtosecond laser fabrication of hybrid micro-optical elements and their integration on the fiber tip, *Proc. SPIE* **7716**, 77160A (2010)
- [A12] M. Malinauskas, V. Purlys, A. Zukauskas, M. Rutkauskas, P. Danilevicius, D. Paipulas, G. Bickaускаite, L. Bukelskis, D. Baltriukiene, R. Sirmenis, A. Gaidukeviciute, V. Bukelskiene, R. Gadonas, V. Sirvydis, and A. Piskarskas, Large Scale Laser Two-Photon Polymerization Structuring for Fabrication of Artificial Polymeric Scaffolds for Regenerative Medicine, *AIP Conf. Proc.* **1288**, 12–17 (2010)
- [A13] M. Malinauskas, V. Purlys, A. Zukauskas, G. Bickaускаite, T. Gertus, P. Danilevicius, D. Paipulas, M. Rutkauskas, H. Gilbergs, D. Baltriukiene, L. Bukelskis, R. Sirmenis, V. Bukelskiene, R. Gadonas, V. Sirvydis, and A. Piskarskas, Laser Two-Photon Polymerization Micro- and Nanostructuring Over a Large Area on Various Substrates, *Proc. SPIE* **7715**, 77151F (2010)
- [A14] P. Danilevicius, M. Malinauskas, M. Rutkauskas, R. Smilingis, A. Zukauskas, G. Bickaускаite, K. Tikuisis, V. Purlys, D. Paipulas, A. Kraniauskas, R. Sirmenis, M. Grishin, A. Michailov, D. Baltriukiene, V. Bukelskiene, R. Gadonas, V. Sirvydis, and A. Piskarskas, Laser 3D microstructuring of biocompatible polymers for biomedical applications, *Rad. Int. Mat. Tech.* 91–93 (2010)

- [A15] A. Zukauskas, M. Malinauskas, K. Belazaras, V. Purlys, G. Bickaускаite, M. Rutkauskas, P. Stanislovaitis, D. Paipulas, R. Gadonas, and A. Piskarskas, Laser multiphoton fabrication of integrated and bifunctional microoptical components, *Rad. Int. Mat. Tech.* 28–31 (2010)
- [A16] M. Malinauskas, V. Purlys, M. Rutkauskas, A. Gaidukeviciute, and R. Gadonas, Femtosecond visible light induced two-photon photopolymerization for 3D micro/nanostructuring in photoresists and photopolymers, *Lith. J. Phys.* **50**(2), 201–207 (2010)
- [A17] M. Malinauskas, G. Bickaускаite, M. Rutkauskas, D. Paipulas, V. Purlys, and R. Gadonas, Self-polymerization of nano-fibers and nano-membranes induced by two-photon absorption, *Lith. J. Phys.* **50**(1, SI), 135–140 (2010)
- [A18] M. Malinauskas, P. Danilevicius, D. Baltriukiene, M. Rutkauskas, A. Zukauskas, Z. Kairyte, G. Bickaускаite, V. Purlys, D. Paipulas, V. Bukelskiene, and R. Gadonas, 3D artificial polymeric scaffolds for stem cell growth fabricated by femtosecond laser, *Lith. J. Phys.* **50**(1, SI), 75–82 (2010)
- [A19] A. Zukauskas, M. Malinauskas, L. Kontenis, V. Purlys, D. Paipulas, M. Vengris, and R. Gadonas, Organic dye doped microstructures for optically active functional devices fabricated via two-photon polymerization technique, *Lith. J. Phys.* **50**(1, SI), 55–61 (2010)
- [A20] M. Malinauskas, H. Gilbergs, A. Zukauskas, V. Purlys, D. Paipulas, and R. Gadonas, A femtosecond laser-induced two-photon photopolymerization technique for structuring microlenses, *J. Opt.* **12**(3), 035204 (2010)
- [A21] M. Malinauskas, A. Zukauskas, V. Purlys, K. Belazaras, A. Momot, D. Paipulas, R. Gadonas, A. Piskarskas, H. Gilbergs, A. Gaidukeviciute, I. Sakellari, M. Farsari, and S. Juodkazis, Femtosecond laser polymerization of hybrid/integrated micro-optical elements and their characterization, *J. Opt.* **12**(12), 124010 (2010)
- [A22] V. Mizeikis, V. Purlys, L. Maigyte, K. Staliunas, and S. Juodkazis, Direct laser writing and applications of dielectric microstructures with low refractive index contrast, *Proc. SPIE* **7927**, 79270F (2011)
- [A23] V. Mizeikis, V. Purlys, W. Inami, and Y. Kawata, Direct laser writing of refractive index micro-structures in lithium niobate, *Adv. Mater. Res.* **222**, 118–121 (2011)
- [A24] V. Mizeikis, V. Purlys, D. Paipulas, L. Maigyte, and K. Staliunas, Tailoring of photonic structures by femtosecond laser lithography, *Proc. SPIE* **8204**, 820417 (2011)
- [A25] M. Oubaha, R. Copperwhite, C. Boothman, A. Ovsianikov, R. Kiyan, V. Purlys, M. O’Sullivan, C. McDonagh, B. Chichkov, R. Gadonas, and B. D. MacCraith, Influence of hybrid organic-inorganic sol-gel matrices on the photophysics of amino-functionalized UV-sensitizers, *J. Mater. Sci.* **46**(2), 400–408 (2011)

-
- [A26] M. Oubaha, R. Copperwhite, A. Gorin, V. Purlys, C. Boothman, M. O’Sullivan, R. Gadonas, C. McDonagh, and B. D. MacCraith, Novel tantalum based photocurable hybrid sol-gel material employed in the fabrication of channel optical waveguides and three-dimensional structures, *Appl. Surf. Sci.* **257**(7), 2995–2999 (2011)
- [A27] N. Vasilantonakis, K. Terzaki, I. Sakellari, V. Purlys, D. Gray, C. M. Soukoulis, M. Vamvakaki, M. Kafesaki, and M. Farsari, Three-Dimensional Metallic Photonic Crystals with Optical Bandgaps, *Adv. Mater.* **24**(8), 1101–1105 (2012)
- [A28] I. Sakellari, E. Kabouraki, D. Gray, V. Purlys, C. Fotakis, A. Pikulin, N. Bityurin, M. Vamvakaki, and M. Farsari, Diffusion-Assisted High-Resolution Direct Femtosecond Laser Writing, *ACS Nano* **6**(3), 2302–2311 (2012)
- [A29] M. Malinauskas, A. Zukauskas, K. Belazaras, K. Tikuisis, V. Purlys, R. Gadonas, and A. Piskarskas, Laser fabrication of various polymer microoptical components, *Eur. Phys. J.-Appl. Phys.* **58**(2), 20501 (2012)
- [A30] M. Malinauskas, D. Baltriukiene, A. Kraniauskas, P. Danilevicius, R. Jarasiene, R. Sirmenis, A. Zukauskas, E. Balciunas, V. Purlys, R. Gadonas, V. Bukelskiene, V. Sirvydis, and A. Piskarskas, In vitro and in vivo biocompatibility study on laser 3D microstructurable polymers, *Appl. Phys. A-Mater.* **108**(3), 751–759 (2012)
- [A31] V. Mizeikis, V. Purlys, D. Paipulas, R. Buividas, and S. Juodkazis, Direct Laser Writing: Versatile Tool for Microfabrication of Lithium Niobate, *J. Laser Micro Nanoen.* **7**(3), 345–350 (2012)
- [A32] M. Malinauskas, A. Zukauskas, V. Purlys, A. Gaidukeviciute, Z. Balevicius, A. Piskarskas, C. Fotakis, S. Pissadakis, D. Gray, R. Gadonas, M. Vamvakaki, and M. Farsari, 3D microoptical elements formed in a photostructurable germanium silicate by direct laser writing, *Opt. Laser. Eng.* **50**(12), 1785–1788 (2012)
- [A33] S. Rekstyte, A. Zukauskas, V. Purlys, Y. Gordienko, and M. Malinauskas, Direct laser writing of 3D micro/nanostructures on opaque surfaces, *Proc. SPIE* **8431**, 843123 (2012)
- [A34] S. Rekstyte, A. Zukauskas, V. Purlys, Y. Gordienko, and M. Malinauskas, Direct laser writing of 3D polymer micro/nanostructures on metallic surfaces, *Appl. Surf. Sci.* **270**, 382–387 (2013)
- [A35] V. Mizeikis, D. Paipulas, V. Purlys, R. Buividas, and S. Juodkazis, Reversible microstructuring of lithium niobate by direct laser write technique, *Proc. SPIE* **8613**, 86130I (2013)

Contributions

The main co-authors of the research results presented in the Thesis are prof. dr. R. Gadonas, prof. dr. K. Staliūnas, prof. dr. V. Mizeikis, dr. M. Farsari, dr. L. Maigytė, dr. M. Peckus and M2 stud. D. Gailevičius.

Prof. dr. R. Gadonas supervised this Thesis.

Prof. dr. K. Staliūnas was a consultant of my PhD studies and supervised the research presented in chapters 5 and 6. He introduced the main concepts of the photonic crystals and their theoretical models.

Prof. dr. V. Mizeikis was a consultant of my PhD studies and supervised the research presented in chapter 4. These results were obtained during the practice in his laboratory in Shizuoka University, Japan.

Dr. M. Farsari gave a lot of practical experience related to photosensitive materials during the practice in FORTH institute, Greece.

Dr. L. Maigytė and dr. M. Peckus are the co-authors of the research presented in chapters 5 and 6. They performed the photonic crystal characterization experiments with the tunable wavelength laser source. L. Maigytė performed numerical FDTD modeling as well as calculations presented in Figs. 6.6, 6.8 and 6.7.

D. Gailevičius is a co-author of the research presented in chapters 5 and 6 and helped in casual work in the lab.

The author of this Thesis has assembled two direct laser writing setups and has created their fabrication software *3DPoli*. This software is used in four laboratories across the world, tens of student bachelor and master thesis, several PhD thesis and was used in more than fifty scientific publications. All the experimental results described in this Thesis were done by the author (except the characterization experiments in chapter 5), as well as a main part of numerical calculations presented in chapter 6 and a part of results presented in chapters 4 and 5.

Structure of the Thesis

The content of the Thesis is divided to six chapters:

- Chapter 1 summarizes the main concepts of photonic crystals, including the explanation of various effects occurring due to temporal or spatial dispersion properties.
- Chapter 2 summarizes the mechanisms of light interaction with the bulk of transparent materials. The principles of microstructure fabrication in the bulk

of the glass and photopolymers are described.

- In chapter 3 the fabrication setups used for the fabrication of photonic crystals are described, including their automation software *3DPoli* and other experimental details.
- In chapter 4 the results of structural colors are presented.
- Chapter 5 summarizes the results of light focusing by flat photonic crystal superlenses.
- In Chapter 6 the results of spatial light filtering by photonic crystals are presented. Chirped and axisymmetric photonic crystals are analyzed and supercollimation effect is reported.

1

Introduction to photonic crystals

Photonic crystals affect the photons in much the same way as solid crystals affect the electrons. They often consist of varying refractive index areas which are periodic in one, two, or three dimensions. The intense research on photonic crystals started in 1987 after the independent works by Eli Yablonovitch [3] and Sajeev John [4], although one dimensional multilayer photonic crystals, such as Bragg mirrors, were known for one hundred years since lord Rayleigh publications [1, 2].

PhCs might possess photonic bandgap – a phenomena, when the propagation of photons is prohibited in all or certain directions. This is probably the best known photonic crystal feature, however there are many more other interesting effects emerging from the possibility to control both temporal and spatial dispersion properties of light. These effects include negative refraction, beam focusing or collimation by flat PhCs, spatial light filtering, superprism or slow light effects. These effects are discussed in the chapter 3 of the Thesis and are covered briefly in this summary as well.

From the practical view of point, PhCs are attractive because of their compact dimensions, mechanical stability and wide application range, however current choice of materials and technologies limit their wider usage. One dimensional photonic crystals are being used for decades in reflection or anti-reflection coatings. Two dimensional photonic crystals are mostly used in commercial hollow fibers. Three dimensional PhCs are the most difficult to fabricate, therefore doesn't have industrial applications yet, however are under intense research.

In spite of several already existing applications, PhCs have just started to be implemented in practice. Humanity are still far behind the nature, which utilizes PhCs in amazingly wide applications for millions of years (the oldest PhCs were found in 47 million year fossils [21]). Surprisingly, natural photonic crystals have drawn

attention only after the works of E. Yablonovitch and S. John, even though Newton has predicted that colors of some birds and insects are caused by light interaction with thin multilayer structures [22].

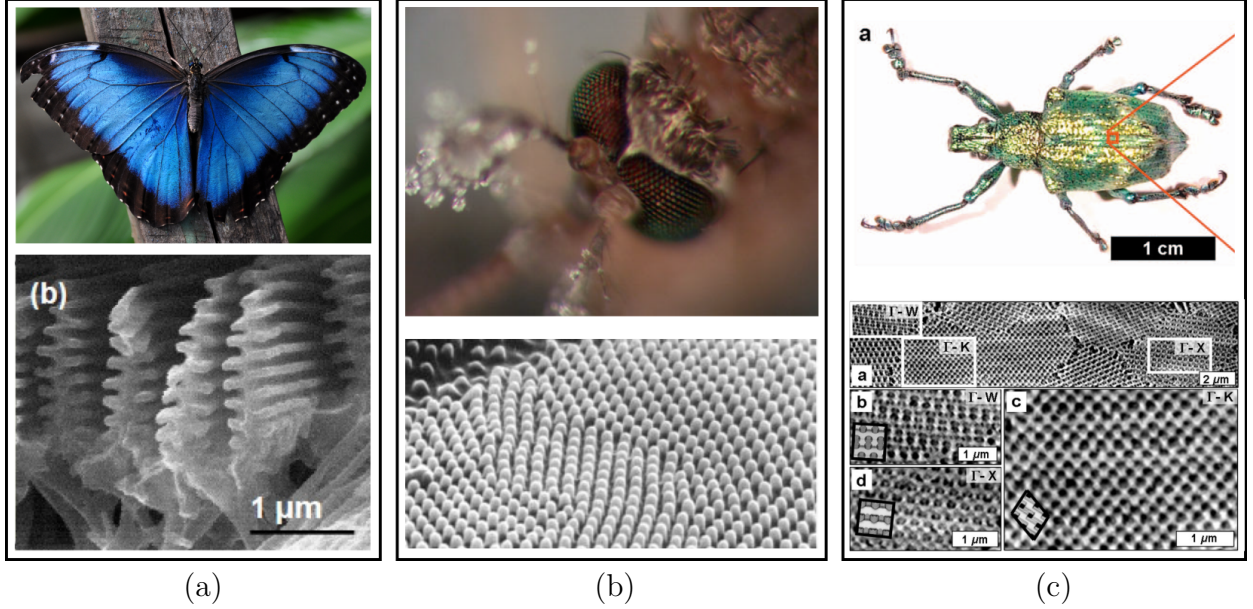


Fig. 1.1: Examples of creatures with natural photonic crystals. (a) The scales of *Morpho* butterfly wings are covered with one-dimensional fir-like multilayer structures, providing bright blue color for wide viewing angles [23–26]. (b) The eyes of Mosquitoes *Culex pipiens* are covered with a two-dimensional array of ~ 100 nm diameter pillars arranged in hexagon lattice, which provides antireflection, self-cleaning and anti-wetting properties [27, 28]. (c) Bright yellowish green color of beetles *Charidotella egregia* are caused by three-dimensional photonic structures having diamond-like lattice [29].

Natural photonic crystals are found in 1D, 2D or 3D forms. They occur in some gemstones, plants, berries, insects, birds, fishes, etc [24, 26, 30]. The main function of PhCs in living organisms is to provide strong vivid colors, which are used for camouflage, warning or various signaling purposes [30]. Such colors have purely physical origin and are called structural colors. Usually they are brighter than pigment colors and do not bleach in time. An example of structural colors are the wings of *Morpho* butterflies (Fig. 1.1 (a)), which possess bright blue color caused by slightly disordered one dimensional fir-like multilayer structures [23–26]. PhCs can be used as anti-reflection coatings as well. Such kind of PhCs were found in the eyes of mosquitoes *Culex pipiens* (Fig. 1.1 (b)), consisting of 2D array of ~ 100 nm diameter pillars arranged in hexagon lattice. Additionally, such anti-reflective surface has self-cleaning and anti-wetting properties [27, 28]. Very complex PhCs were found in *Lamprocyphus augustus* beetles (Fig. 1.1 (c)). Their yellowish green color is caused

by 3D chitin microstructures, with lattice geometry following the diamond lattice [29]. Interestingly, such PhCs were proposed theoretically before their discovery in nature [31]. Sometimes natural PhCs might have properties which are not used in nature, e.g. the wings of *Morpho* butterflies were found to be sensitive to mid-infrared radiation and chemical agents, therefore were proposed for sensing purposes [18, 32].

Inspired by nature scientists try to mimic natural structural colors in artificial photonic structures [33, 34]. Such colors are also demonstrated in chapter 4.

1.1 Temporal dispersion effects in photonic crystals

Due to periodic nature of PhCs, every Bloch wave represented by certain k vector can possess discrete energy spectrum only, meaning that each point of k space has it's own energy spectrum. If at certain energy region there are no allowed states at any k vector, then this region is called a photonic bandgap. If the bandgap exists in certain directions only, it is called pseudo bandgap. An example of bandgaps in PhCs and solid crystals are given in Fig. 1.2.

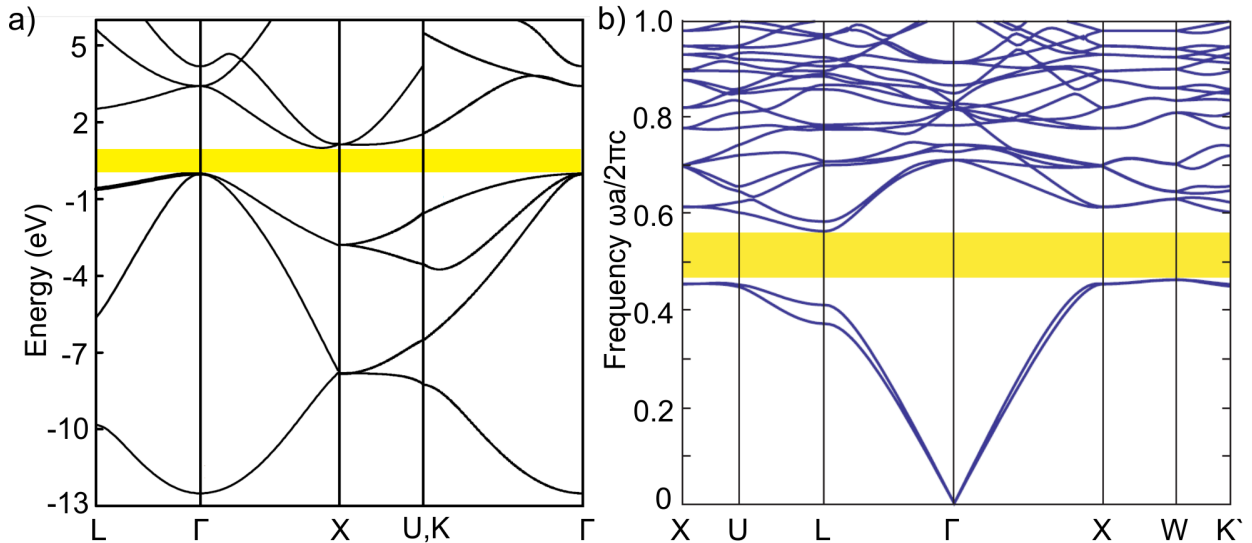


Fig. 1.2: Example of bandgaps (yellow region) in (a) silicon [35] and in (b) woodpile photonic crystals [36]. Both types of crystals are arranged in diamond-like lattice.

Photonic bandgap is determined by temporal dispersion properties of PhCs. Temporal dispersion might also invoke another phenomenon, called slow light effect. Slow light effect can be realized in various systems, including PhCs. It allows to slow down the effective velocity of light up to meters [37, 38] or even millimeters [39] per second.

The physical origin of the effect is based on multiple interference and occurs at low slopes of dispersion curves. Since the group velocity $\vec{v}_g = \nabla_{\vec{k}}\omega(\vec{k})$ is dependent on the gradient of frequency, the low slope of frequency gradient results in low group velocity and thus slow light.

Slow light prolongs the duration of light–matter interaction, therefore it could be used in sensing applications. Additionally, it compresses the light pulses and increases their intensity [40]. Devices, based on slow light effect, might be used in all-optical computing where optical buffer memory is required. Currently, very long fiber coils are used for this purpose [41]. At the slow light medium boundary there is a strong mismatch between the velocities of Bloch modes causing large coupling losses, which could be avoided by using special adiabatic couplers [42].

1.2 Spatial dispersion effects in photonic crystals

Spatial dispersion engineering offers the possibility to control the light propagation in PhCs. Various effects, such as negative refraction, flat lensing, super collimation, superprism and spatial light filtering are based on spatial dispersion properties. Next we will briefly discuss these phenomena using isofrequency contours.

Super lensing effect is caused by negative refraction of light. Such anomalous refraction might be created by convex curved isofrequency contours, such as depicted in Fig. 1.3 (a) (for guidelines how the isofrequency contours are interpreted see the main text of the Thesis). It has been proven that flat super lenses has greater resolution than conventional lenses, where the resolution is limited to approximately the wavelength [12, 43–48]. When the isofrequency contours are flat, the supercollimation effect occurs [5–10]. In this case, the light beams can travel unlimited distances without diffractive spreading or focusing. Strongly curved isofrequency contours might cause another effect, called superprism effect. Superprisms are extremely sensitive to the light wavelength or it's direction devices. The sensitivity of superprisms can be ~ 500 times larger than the sensitivity of conventional prisms [49]. Spatial light filtering might also be achieved in PhCs by forbidding the light propagation in certain directions. There might be two cases: with [14, 50–53] and without [15] the angular bandgaps, in the latter case the light is deflected to diffraction maxima. This case is studied more in detail in chapter 6.

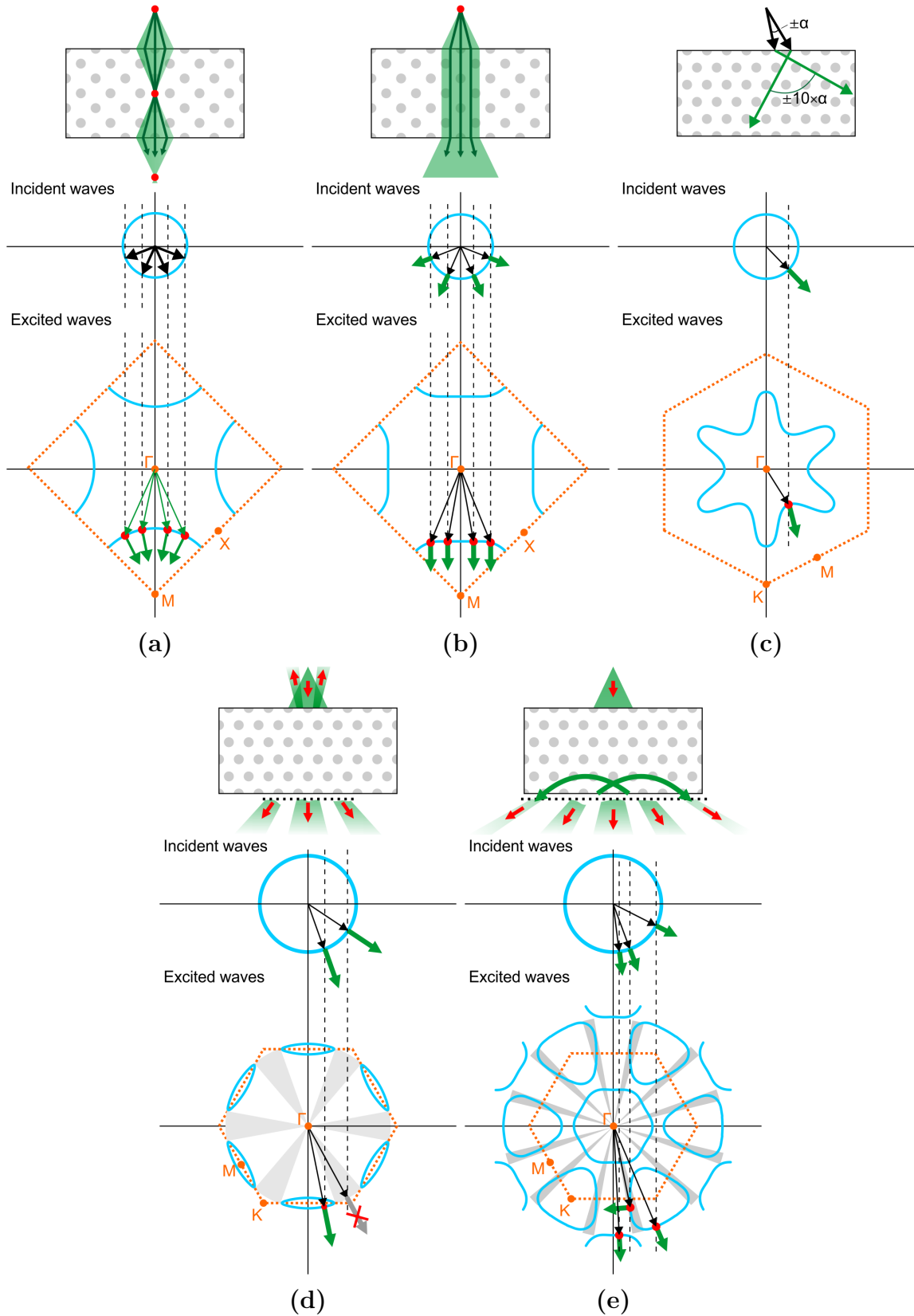


Fig. 1.3: Spatial dispersion effects in photonic crystals: (a) superlens effect, (b) supercollimation effect, (c) superprism effect, (d) spatial light filtering with and without (e) angular bandgaps. The blue curves denote isofrequency contours, thin lines represent phase velocity direction, while thick lines – group velocity. Orange dotted lines mark first Brillouin zone and black dotted lines mark the tangential vector components which are of a constant length.

2

Principles of transparent materials laser fabrication

Just a couple of years after the creation of the laser in 1962 [54], it was noticed that intense Q-switched laser beam can cause modification or damage of various materials, particularly breakdown of optical elements used in lasers. Such phenomena were initially considered to be harmful, having no practical value, and preventing further development of lasers. However, it was soon understood that lasers can be used in industry as a highly accurate, non-contact welding or cutting tools, i.e. they can process materials surface. It took a couple of decades more in order to understand that lasers can do what any other mechanical tool can't – they can also process the volume of transparent materials without affecting their surface [55].

Transparent materials has a bandgap larger than the incident photon energy, hence the photon energy is not sufficient to transfer electrons from the valence band to the conduction band. Such materials do not absorb light, therefore at the first glance it seems rather impossible to process them by using the laser beam. However, it is possible to overcome this limit by utilizing nonlinear phenomena, which often occur at the focal volume of tightly focused femtosecond laser beams, where huge peak intensities occur. The first demonstration of such possibility was shown in 1996, where waveguides were inscribed to the bulk of various glasses (doped with germanium, boron, sodium, calcium, fluorine, zirconium) using femtosecond Ti:Sapphire system (810 nm, 120 fs, 200 kHz). It was shown that refractive index change of the order of 0.01–0.035 is achievable in all of these glasses, which is sufficient for optical waveguides [56].

In 1997, soon after the previous publication, another publication came out [57], demonstrating the possibility of creating three-dimensional microstructures in the bulk of light sensitive photopolymers. Such polymers, composed typically of a mix-

ture of monomers and a photosensitizers, are sensitive to UV light. If exposed, the chemical reactions start, which lead to polymerization of monomer molecules. These reactions can also be initiated nonlinearly using near infrared femtosecond laser radiation. The light is absorbed via multi photon absorption, therefore this technology was named two photon or multi photon polymerization. The inscribed microstructures are highly chemically resistant, therefore they can be revealed by washing out the unexposed areas with solvents. The example structures of the mentioned pioneering publications are shown in Fig. 2.1.

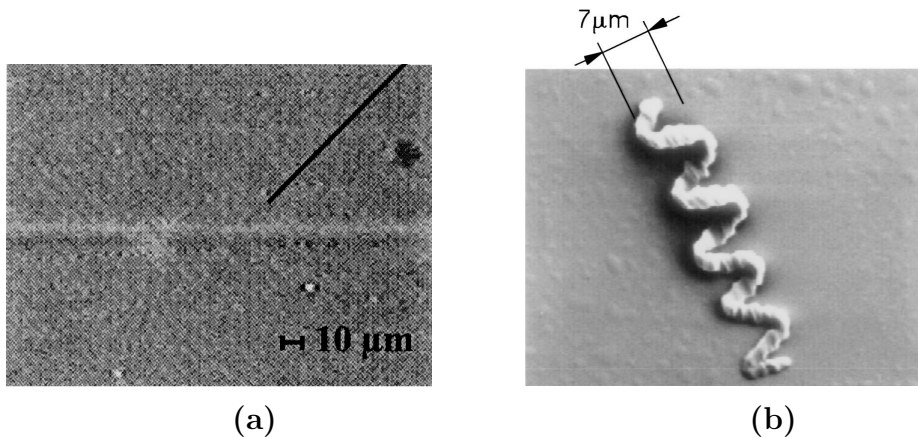


Fig. 2.1: Examples taken from the pioneering works demonstrating the possibility to inscribe the microstructures in the bulk of (a) the glass and (b) photopolymers, by using tightly focused femtosecond laser beam. (a) An optical image of laser-inscribed waveguide [56], (b) scanning electron microscope micrograph of three-dimensional polymeric 7 μm wide spiral, made by two photon polymerization technique [57].

The second chapter of the Thesis reviews the mechanisms of light–matter interactions in transparent materials. It is shown, that every modification of the bulk might be divided into the three main steps – generation of electron plasma, energy relaxation and material modification. Each step is described more in detail, the role of ultrashort pulses is discussed. Next the principles and main concepts of multiphoton polymerization technology are summarized.

3

Experimental details of fabrication setups and materials

¹ Both multiphoton polymerization and glass bulk modification technologies, discussed in the first chapter of the Thesis, could in general be called *Direct Laser Writing* technologies, as both share the same point-by-point modification principle. Therefore, the experimental realization of both technologies is almost identical, in spite of their different physical nature. In this chapter of the Thesis the experimental details of such microstructure fabrication systems are provided.

3.1 Three-dimensional microfabrication systems

The main components of point-by-point laser fabrication systems include the laser, sample translation stages and control software. In Fig. 3.1 (a) the optical circuit of example microfabrication system, assembled during this work, is depicted. Yb:KGW laser („Pharos“, Light Conversion) was used as a laser source, having variable repetition rate of 1 – 200 kHz, maximum average power of 6 W, and 1030 nm wavelength. The precise power of the laser beam is set by two sets of attenuators, consisting of half-wave plate and a pair of polarizers. If necessary, the beam could be guided to second harmonic generation circuit by removable mirrors V1 and V4. Next the beam is expanded by 3 times using Galilean telescope in order to fill entire aperture of microscope objective. Expanded beam is passed to galvoscanning mirrors and then to the microscope objective through 4F system (L3, L4). The microscope objective focuses the light to the glass or photopolymer sample, which is positioned by three-dimensional translation stages. The live-view imaging is achieved by illuminating the sample with red light emitting diodes, and collecting the light with tube

¹The fabrication systems described in this chapter were used in [A1-A36] publications.

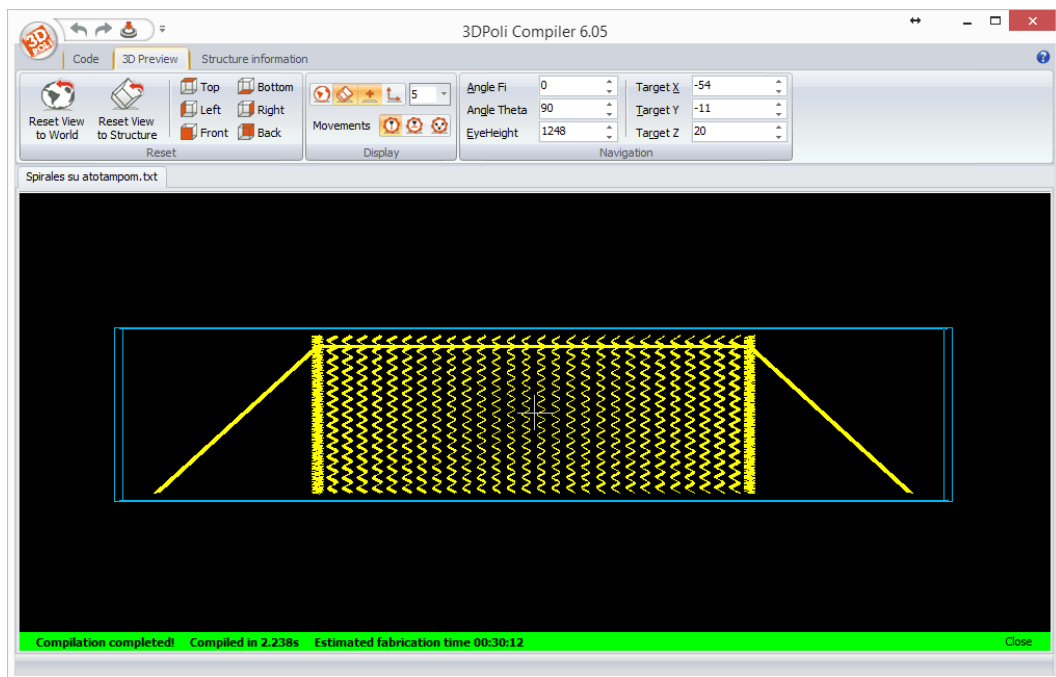
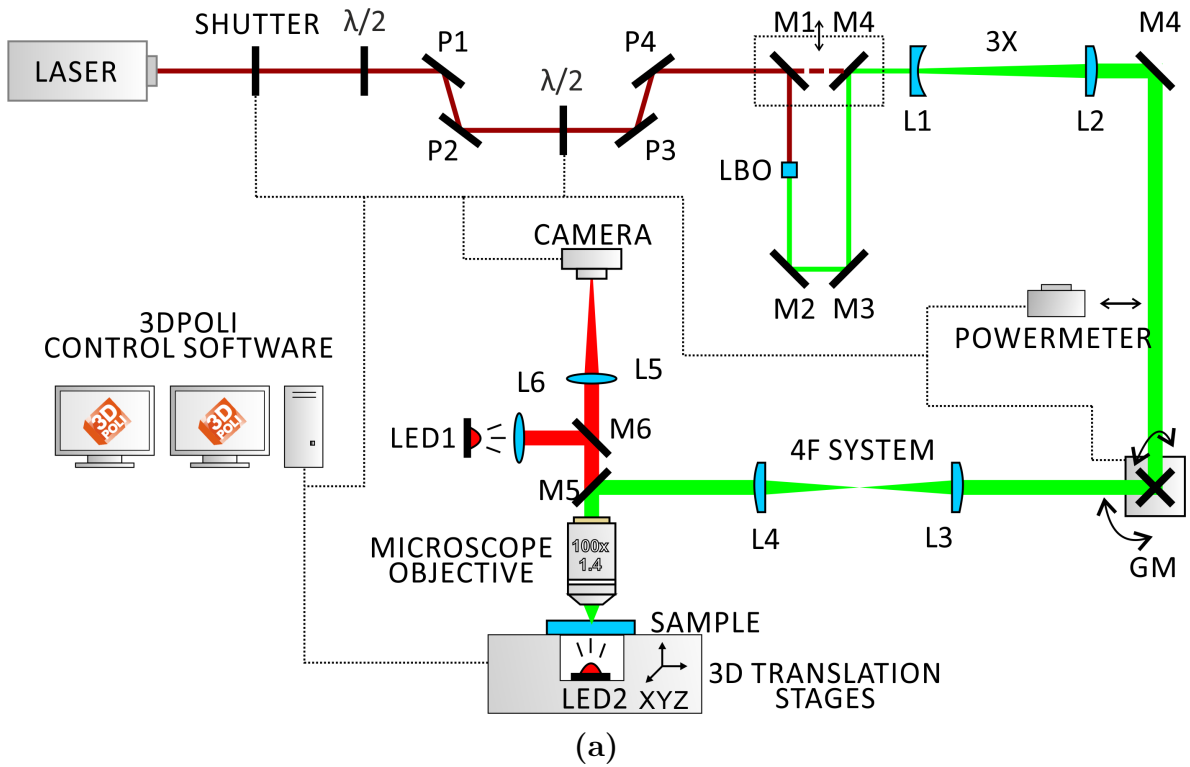


Fig. 3.1: (a) The optical circuit of direct laser writing fabrication setup. See the main text for details. (b) *3DPoli* fabrication software window demonstrating the 3D preview of designed spiral array structure.

lens L5 to the digital camera.

The fabrication software is crucial component of direct laser writing technology. The capabilities of the software limits the variety and complexity of possible structures, as well as productivity of the work-flow. In practice, each microfabrication system consist of different equipment, so there are no commercial software suitable for every system, therefore home-made software must be used. During this PhD work the *3DPoli* microfabrication software was created.

3DPoli is a software designed for both the definition of the microstructures and for their fabrication. The structures in *3DPoli* are defined via various commands, which include positioning commands, cycles, variables, procedures, mathematical functions and so on. Additionally, predefined structures may be imported from standard lithography files. Before the fabrication, the microstructures can be visualized in 3D preview (Fig. 3.1 (b)) and various automatically calculated parameters may be inspected. One of the main features of this software is it's compatibility with various equipment, which is achieved by modular design of the software.

This chapter of the Thesis describes the microbarication setups and *3DPoli* more in detail, provides the description of photochemical reactions and synthesis of hybrid organic-inorganic sol-gel photopolymer, which was used in the photonic crystal fabrication via multiphoton polymerization, and describes other additional equipment, required for the fabrication of photonic crystals and other microstructures. Some examples, created with described systems and fabrication software are given in Fig. 3.2.

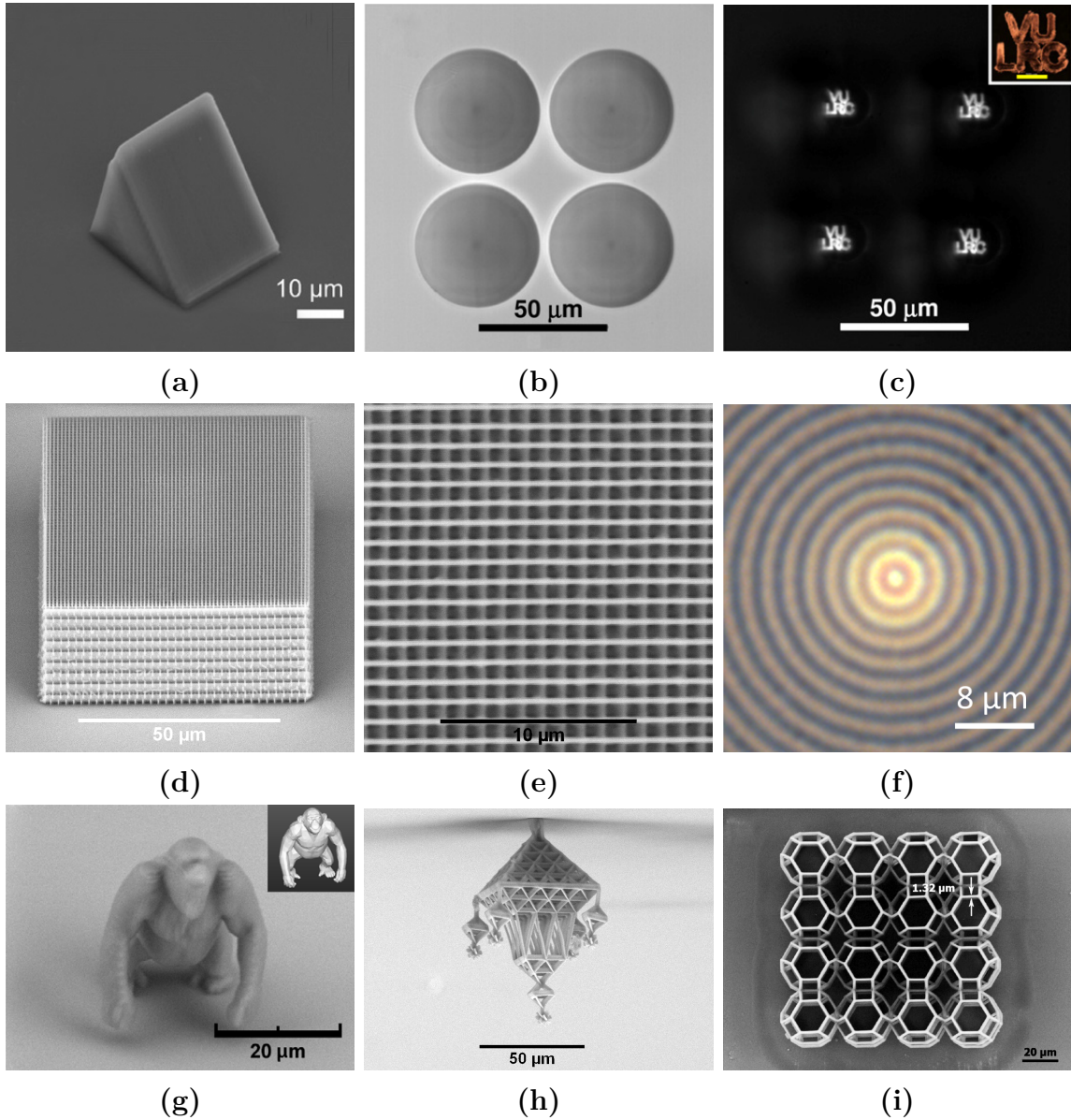


Fig. 3.2: Examples of microstructures, created with *3DPoli* software and fabricated by direct laser writing setups described in this chapter of the Tesis. Micro-optical components: (a) microprism [A32] (b) microlens array and (c) their imaging performance [A21]. Photonic elements: (d) photonic crystal made of hybrid organic-inorganic tantalum containing photopolymer (e) and its surface [A26], (f) axisymmetric photonic structure inscribed in the bulk of the glass. (g) Microgorilla, which model was imported from STL file [A9]. (h) traditional lithuanian straw himmeli made of photopolymer. (i) Scaffold for cell growth [A18].

4

Structural colors in woodpile photonic crystals

¹ Structural colors were first discovered in natural systems, such as gemstone opal, blue wings of *Morpho* butterflies, colorful scales of fish, and insects, etc. [24, 26]. Bright, non-fading coloration of purely physical origin not related dyes or pigments are of interest for a wide range of applications [18, 32, 34], and replication of structural color in periodically structured dielectrics has attracted some attention recently [23, 33]. Structural colors in dielectrics are associated with photonic band gap (PBG) or photonic stop/pseudo gap (PSG) of photonic crystals [58]. Strong resonant reflectance bands due to PBG or PSG may lead to coloration, provided that central wavelength of the PBG/PSG spectral region is tuned to the visible wavelength range.

Fabrication of structural color materials relies on availability of fast and accessible, natively 3D nanostructuring techniques, such as Direct Laser Writing (DLW) lithography, described in chapters 1 and 2. In many PhCs fundamental (lowest frequency) PBG or PSG typically open between lower photonic bands at normalized frequencies $f = a/\lambda \approx 0.5$, where a is the PhC lattice period and λ is the wavelength. In order to tune the fundamental stop gap to the visible spectral range, PhC lattice period must be scaled down to $a \approx \lambda_{PBG}/2 \leq 500\text{nm}$, with average feature size approaching 100 nm. Such spatial resolution is difficult to achieve without major improvements [59] to the DLW technique. High resolution requirement may be circumvented by exploiting higher-order PSG, as demonstrated for 3D woodpile architecture PhCs fabricated by DLW [60, 61]. However, in this case the face-centered-cubic (*fcc*) unit cell of woodpile structure must be stretched toward the face-centered tetragonal (*fmt*) symmetry. Tuning PSG to the visible spectral range would require very short lattice periods along non-stretched lattice directions, which is difficult to achieve in practice. In this study we demonstrate 3D woodpile PhC structures having *fcc* lattice

¹Chapter is based on [A6] ir [A7] publications.

symmetry and relatively large transversal period of $\approx 0.6 - 1 \mu\text{m}$ exhibiting structural color and realized in photoresist using DLW technique. The origin of the observed structural colors is not completely clear as it can not be directly explained by higher order PSG.

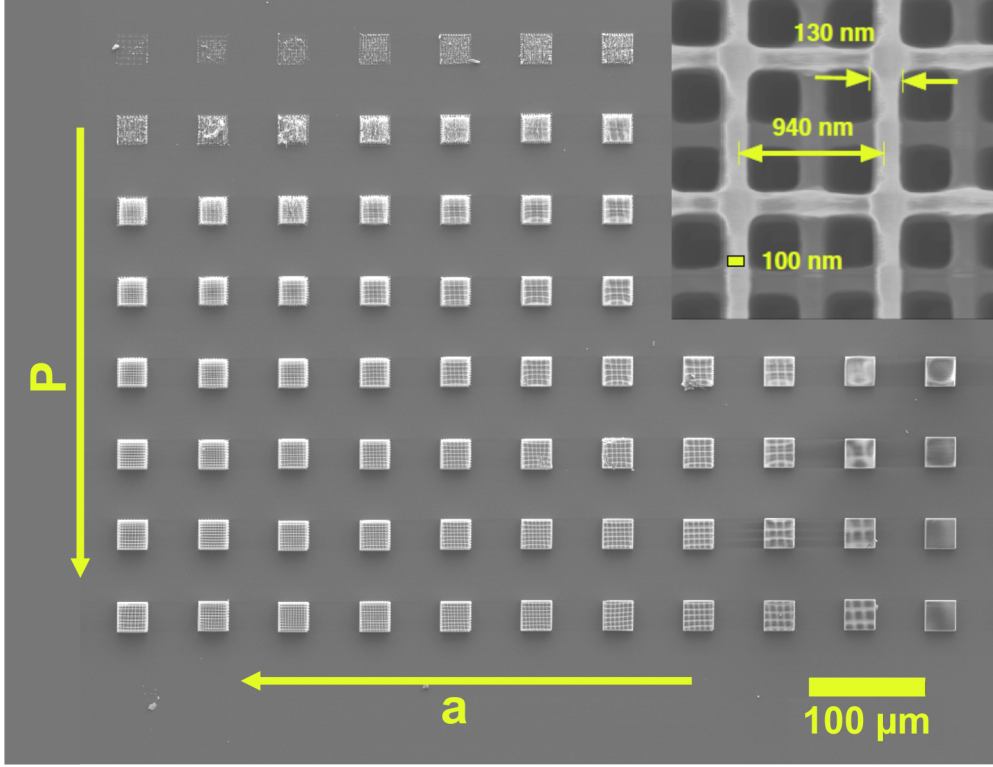


Fig. 4.1: Scanning electron micrograph of an array of photonic crystals made with varying laser fabrication power (P) and lattice constant (a). The inset shows magnified view of one of the crystals.

Photonic crystals of woodpile geometry were fabricated by using DLW setups described in 2 chapter. Figure 4.1(a) shows scanning electron (SEM) image of an array of woodpile structures, each having a footprint of $25 \times 25 \mu\text{m}^2$ and a total height of $N = 25$ layers, fabricated using various combinations of in-plane fcc lattice period a_{xy} and writing laser power P_{DLW} in order to systematically tune spectral position of the PSG region via the lattice period and dielectric filling fraction. Figure 4.2(a) shows optical reflectance image of such PhC array. The brightest colors can be found in vicinity of diagonal line connecting top-left and bottom-right corners of the matrix. Illumination and imaging was done using halogen lamp illumination and $\text{NA}=0.3$ microscope lens, which integrates reflectance within about $\pm 17^\circ$ spatial angle with respect to the normal to the sample surface (woodpile stacking direction).

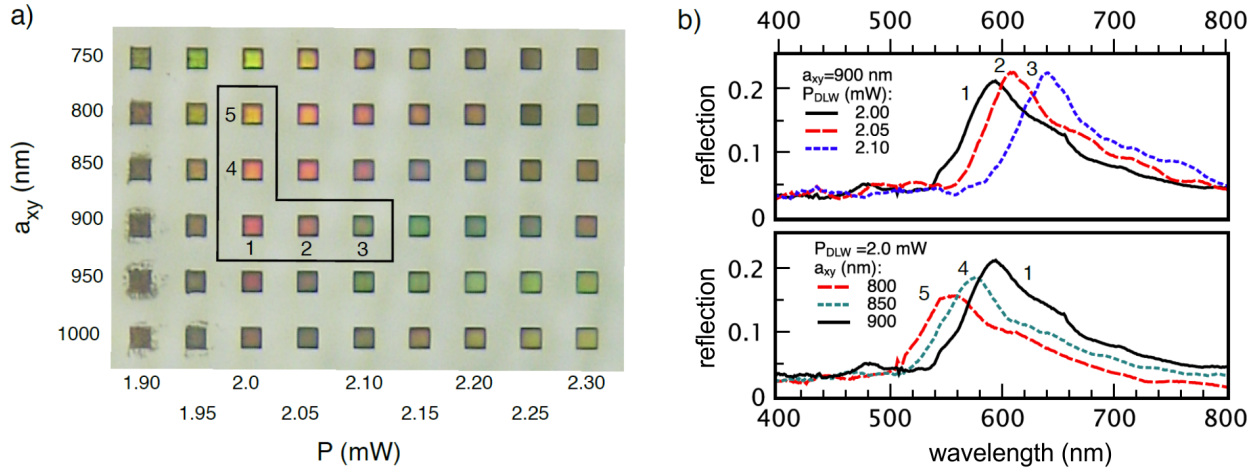


Fig. 4.2: (a) Optical microscopy image of woodpile photonic crystal samples with various lattice parameters and fabricated using various laser powers, (b) visible reflectivity spectra of samples denoted by numbers in (a).

Under these circumstances, observation of well-defined color indicates its relative independence of the observation angle. However, under observation with $NA > 0.5$ lens, the colors were found to fade, blending into bright white.

Reflectance spectra of selected samples emphasized by line in Fig. 4.2(a) are shown in Fig. 4.2(b). The spectra were measured in the range of 250-800 nm using FE-3000 microscope (Otsuka Electronics) with $NA=0.4$ imaging lens. Clear reflectance peaks with magnitude of $\sim 20\%$ are seen; the peaks exhibit red-shift with P_{DLW} (increasing dielectric filling ratio) and the PhC lattice period in accordance with Maxwell's scaling behavior [36]. Spectral positions of the peaks roughly correlate with colours of the samples, although for the sample with $a_{xy} = 900$ nm and $P_{DLW} = 2.10$ mW, greenish color seems to contradict its reflectance peak centered around 640 nm wavelength. This is most likely due to spectral variation of the halogen lamp illumination.

Colourful fcc woodpile PhC structures fabricated in photoresist by advanced DLW technique were reported previously [59]. However, structures prepared in the present study have lattice period about twice larger than those in Ref. [59], but nevertheless exhibit visible coloration. In fact, theoretical analysis based on the the PhC lattice parameters suggests that their fundamental PSG should open at near-infra-red (NIR) wavelengths (see below). To verify this expectation, in addition to the visible reflectance, NIR reflectance of some samples was measured using Fourier-Transform Infra-Red (FTIR) spectrometer (Nicolet Nexus with Continuum infrared microscope). Samples prepared for FTIR measurements had larger area of $50 \times 50, \mu\text{m}^2$ to improve signal collection. Optical reflectance images (Fig. 4.3(a)), and extended

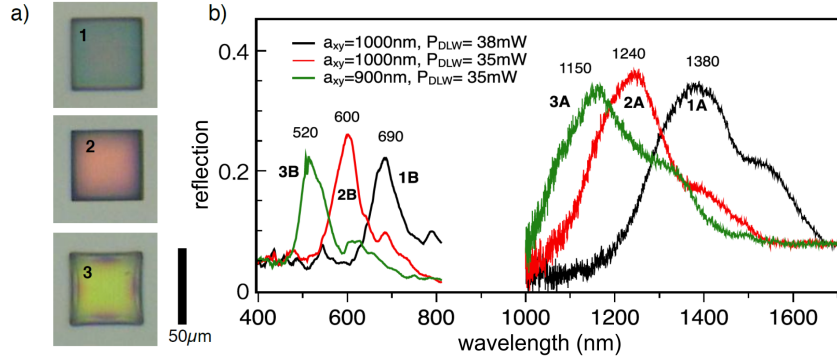


Fig. 4.3: (a) Optical images and colors of PhC samples, (b) their reflectivity spectra at visible and NIR wavelengths. Approximate central wavelengths of NIR reflectance peaks 1A, 2A, and 3A and visible peaks 1B, 2B and 3B are indicated by numbers (in nanometers).

reflectance spectra of three PhC samples (Fig. 4.3(b)) illustrate that in addition to visible colors, NIR reflectance peaks can be seen. The NIR peaks are labeled as 1A, 2A, and 3A according to the sample numbers in Fig. 4.3(a). The NIR peaks are matched by reflectance peaks at visible wavelengths labeled as 1B, 2B, and 3B. From the peaks' central wavelengths given in the plot one can see that in each sample peak B occurs at approximately twice shorter wavelength than peak A. Such relationship seemingly suggests that visible reflectance peak B responsible for the structural color is due to a second-order PSG.

However, according to theoretical simulations, second-order PSGs do not open in these samples. Simulations of photonic band diagrams using MIT Photonic bands software [62], and simulations of reflectance spectra using Finite-Difference Time-Domain (FDTD) software (FDTD Solutions, Lumerical) were performed using structural parameters of the samples extracted from Scanning Electron Microscopy (SEM) images, such as those shown in Fig. 4.4(a). The lateral parameters $a_{xy} = 940$ nm and $d_{xy} = 130$ nm for sample 1 (Fig. 4.3(a)) were directly determined from SEM images, and reflect photoresist shrinkage by about $\approx 5\%$, a typical amount for zirconium-based sol-gel composites [63]. The axial parameters a_z and d_z were inferred from their fixed relationships with a_{xy} and d_{xy} . SEM images also illustrate high porosity (low dielectric filling fraction) of the colourful samples.

Figure 4.4(b) summarizes the results of reflectivity calculations along woodpile layer stacking direction, or $\Gamma - X'$ crystallographic direction. As can be seen, spectral positions of experimental peaks A and B are qualitatively reproduced by the calculations. Simulations also predict high reflectance regions at short wavelengths, but in the experimental spectra these high-frequency features typically become suppressed.

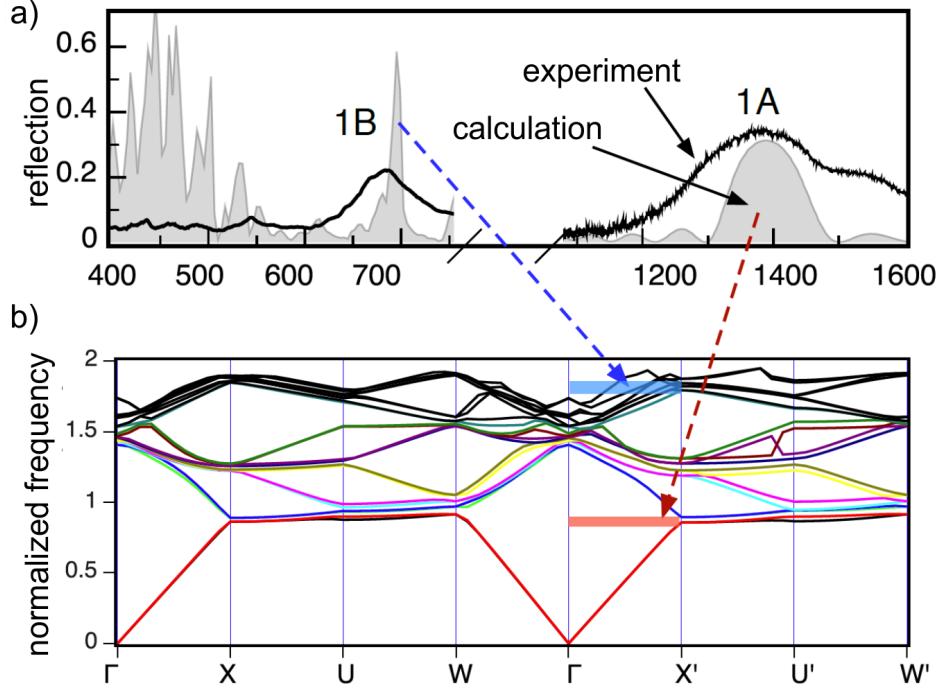


Fig. 4.4: (a) reflectance spectrum of a model structure with lattice parameters estimated from Fig. 4.1 (b), and experimentally measured spectrum, (b) photonic band structure of the model structure.

sed due to subwavelength-scale disorder (e.g., photoresist surface roughness). High-reflectance band is also expected to occur in the wavelength range of 800-1000 nm, but since this range was not available for measurements, it is also omitted in the simulated spectrum.

Photonic band diagram shown in Fig. 4.4(c) uses normalized frequency units $f_n = a/\lambda$, where $a = \sqrt{(2)}a_{xy}$ is the lattice period of fcc unit cell. Correspondence between wavelengths of the reflectivity peaks and frequencies in the band diagram is emphasised by arrows. As can be seen, the NIR reflectivity peak 1A corresponds to the fundamental PSG along the $\Gamma - X'$ direction seen at $f_n = 0.93$. On the other hand, the visible reflectivity peak 1B does not have a matching frequency gap in the band diagram along the same direction. Therefore, while the NIR reflectivity peak can be associated with the fundamental PSG, physical origin of the visible peak is apparently not directly related to PSG.

Photonic crystals may exhibit strong optical attenuation and high reflectivity regions even in the absence of PBG or PSG due to poor coupling and group velocity mismatch between fast incident plane waves and slow Bloch modes in photonic crystal. In order to verify possible role of slow light in our samples, we have examined group velocity dispersion along the $\Gamma - X'$ direction. Group velocity is defined as

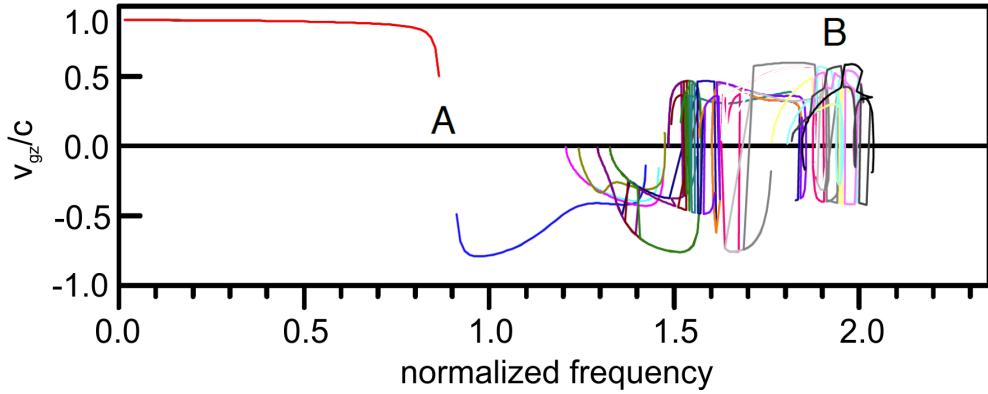


Fig. 4.5: Calculated dependence of group velocity v_{gz} on normalized frequency along $\Gamma - X'$ direction. Different colors represent different photonic bands.

$v_g = d\omega/dk$, where ω is the cyclic frequency, and approaches zero in horizontal segments of photonic bands. Since we are primarily interested in propagation properties along the woodpile stacking direction z , it is enough to consider behavior of the group velocity component parallel to the z axis, v_{gz} . The software used for band structure calculations allows to obtain frequencies $f(k)$ or $\omega(k)$ of the Bloch modes, and the corresponding group velocities $v_g(k)$. From these dependencies $v_{gz}(f)$ dependence was obtained, and is plotted in Fig. 4.5. Group velocity decreases slightly near the edge of the Brillouin zone in vicinity of the fundamental PSG, where NIR reflectance peaks (denoted as A1, A2 and A3 in Fig. 4.3) were observed. However, main reason for these peaks is presence of the frequency gap rather than slow light. Above the PSG, $v_{gz}(f)$ changes the sign, reflecting negative slope of photonic bands (we stress here, that negative values of group velocity component do not imply presence of negative refraction, for which phase and group velocity vectors must be anti-parallel). Above the PSG, especially for $f \geq 1.45$ group velocity tends to exhibit fast oscillations between positive and negative values, crossing the $v_{gz}(f) = 0$ point. We regard density of these crossovers as a qualitative measure of the density of states with low group velocity. As can be seen from the Figure, there are two spectral regions with high crossover density at $f = 1.55 - 1.6$ and at $f = 1.8 - 2$. The first region is centered near the wavelength of $\lambda \approx 0.85 \mu\text{m}$ where experimental reflectivity was not measured (but calculations reveal a high reflectance band), and the second region is centered near the wavelength of $\lambda \approx 0.7 \mu\text{m}$, i.e., close to the visible high-reflectance region 1B on sample 1. This correspondence can be also extended to other samples with different lattice periods and dielectric filling fractions via Maxwell's scaling. Hence, the above analysis supports assumption that slow light phenomenon may be responsible for the observation of structural colors in our samples.

Conclusions

In conclusion, we have presented experimental data and analysis suggesting the possibility to obtain structural colors in polymeric photonic crystals due to modified dispersion of high-frequency photonic bands, rather than due to the fundamental photonic stop gap. This allows one to obtain structural colors in photonic crystals with relatively large unit cell, thus substantially decreasing the requirement of high spatial resolution, and making fabrication of such materials by DLW technique somewhat easier. Previously, exploitation of higher-order PSGs in 3D woodpile architecture polymeric photonic crystals was suggested as a possible method to allow larger lattice period and easier fabrication [61]. However, in order to achieve multiple higher-order PSGs, strongly elongated fcc unit cell was used. Since elongation pulls down frequencies of fundamental and higher-order PSG, it is difficult to tune them to the visible wavelength range by downscaling the fcc unit cell, because very high lateral resolution of DLW fabrication would be still required. Here we have presented a more practical alternative to obtain structural colors without PSG and maintaining the fcc unit cell symmetry. This result may be helpful in realization of dielectrics with controllable structural colors by DLW and other techniques.

Beam focusing by woodpile photonic crystals

¹ Spatial periodic modulation of the refractive index on a wavelength scale in photonic crystals (PhCs), provides control of both temporal and spatial dispersion properties of light waves, in the latter case offering the possibility of manipulating the spatial propagation of the light beams. PhCs may provide, for particular geometries, anomalous spatial dispersion for a beam propagating inside the structure [44], leading to nondiffractive (self-collimated) propagation of light [10] and negative refraction [46, 64], and also to flat PhC lensing [45] or superlensing [65] effects. See more in 1.2 chapter.

The concept of flat PhC lensing is based on the transformation of the phases of the angular field components. The convex-curved phase shifts of field components accumulated during propagation inside the PhC can be compensated by the usual concave-curved phase shifts during propagation in a homogeneous material, both in front of and behind the PhC, resulting in focusing behind the PhC. The distance between the object and the PhC, l_1 , and between the PhC and the image, l_2 , obey the relation $l_1 + l_2 = F$, where F is the focal distance of the flat PhC lens. This is in contrast to the usual focusing by conventional or by Fresnel lenses, where the well-known relation $1/l_1 + 1/l_2 = 1/F$ holds (Fig. 5.1).

In this chapter a full two-dimensional focusing by a polymer-based three-dimensional woodpile PhCs is experimentally demonstrated. Full two-dimensional flat lens focusing has been experimentally shown for microwaves [5] and for sound waves [66]. Moreover, even 1D focusing/imaging by PhC slabs has thus far been experimentally demonstrated only in the near-IR frequency range [67].

PhC lensing is usually considered for modulation periods of the order of wavelength. Flat lensing occurs due to the convex-curved spatial dispersion (or isof-

¹Chapter is based on [A2] publication.

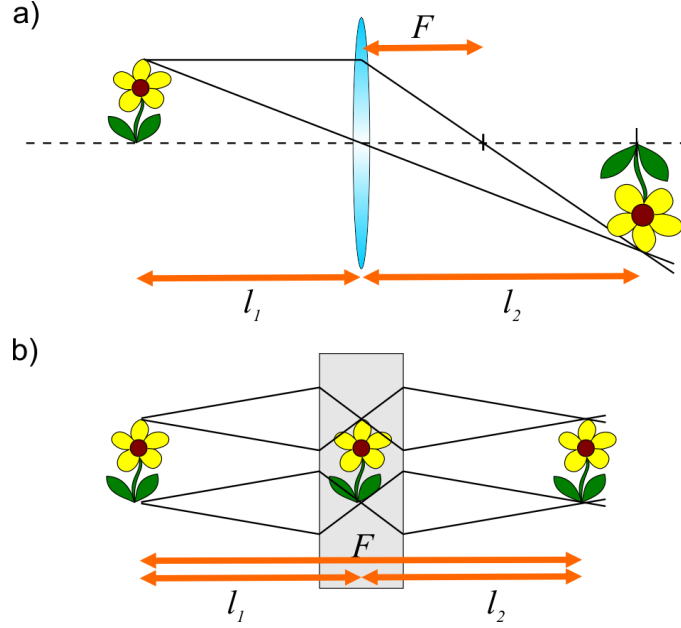


Fig. 5.1: Focusing by (a) conventional and (b) super lenses. Object placed at l_1 distance is images at the distance l_2 . F denote focal length.

frequency) lines in the first, or at most in the second, propagation band. In particular, for PhCs of square symmetry, the corner of the Brillouin zone (BZ) is positioned at $\lambda_{1BZ} = 2\bar{n}d_0$ (λ is the wavelength, \bar{n} is the effective refractive index of the PhC, and d_0 is the lattice period). The self-collimation (SC) (the flattening of the spatial dispersion lines) occurs at frequencies below the corner of the BZ, i.e., at $\lambda_{SC} > \lambda_{1BZ}$. The flat lensing, which is based on anomalously curved spatial dispersion lines, generally occurs between the frequencies of SC and of the edge of the BZ. The experimental demonstration of flat lensing in the visible range is therefore a difficult task, due to technological limitations of PhC fabrication techniques at this scale. We use an alternative approach based on PhCs with relatively large modulation periods, but searching the flat lensing effects in higher order bands. This, on one hand, simplifies the fabrication of the samples, but on the other hand makes the observation and interpretation of the focusing effect more complicated, since the harmonic expansion techniques become very complicated in high-order propagation bands.

Finite-difference time-domain (FDTD) calculations were first performed in order to check the expected focusing of a Gaussian beam. The parameters were as follows: refractive index $n = 1.5$, transverse period $d_{\perp} = 0.9 \mu\text{m}$, longitudinal period $d_{\parallel} = 6 \mu\text{m}$ (filling factor 70%), transverse size $80 \mu\text{m}$, and length of the crystal $30 \mu\text{m}$ (5 longitudinal periods). The beam was focused just at the front face of the PhC, with the focal spot width in the range of $1.6 - 3.0 \mu\text{m}$.

First we identified the SC wavelength, by propagating the narrow beam inside

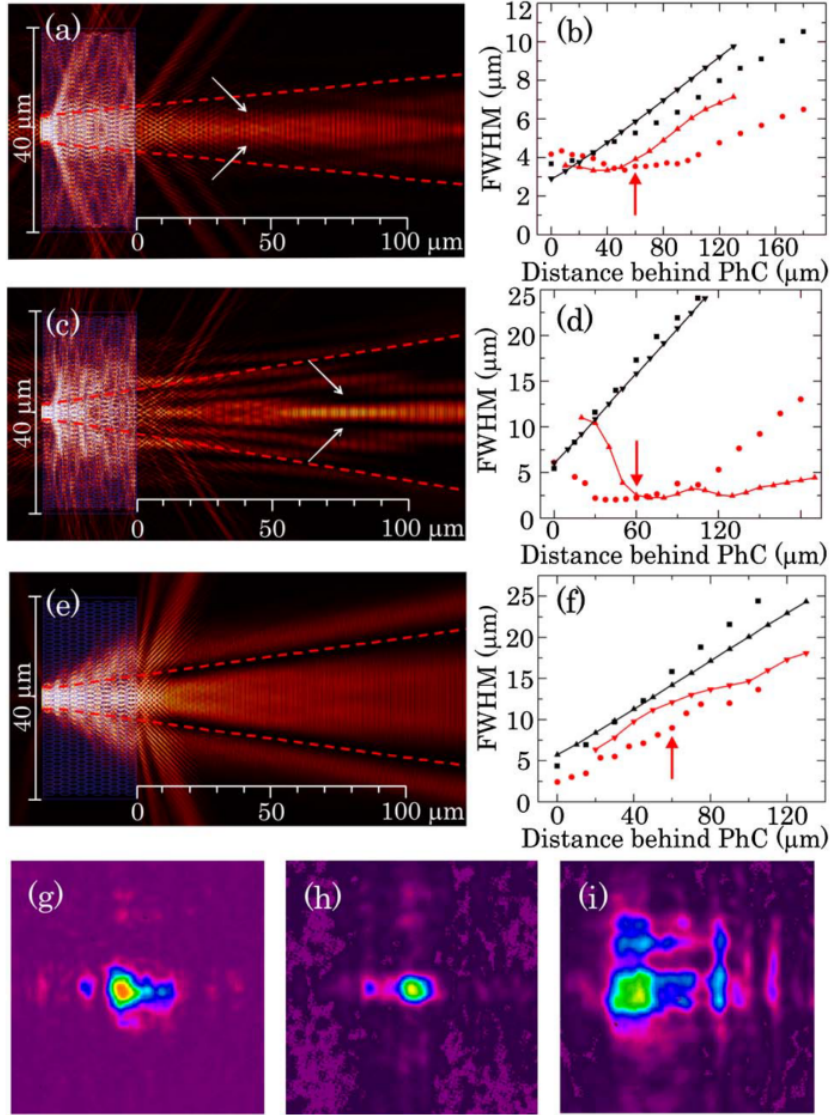


Fig. 5.2: (a), (c), (e) Field intensity distributions at 532, 570, and 700 nm, inside and behind the PhC, calculated by 2D FDTD; (b), (d), (f) the beam width depending on distance behind the crystal (red) compared to the width of the reference beam (black) (dots, experimental results; lines, numerical results); (g)–(i) 2D distributions of the beams at the plane of 60 μm behind the PhC taken with a CCD camera for the corresponding wavelengths of 532, 570, and 700 nm (corresponding positions are marked by arrows in (b), (d), and (f), respectively).

the elongated woodpile structure (20 longitudinal periods), at around $\lambda_{SC} = 610$ nm. We concentrated, consequently, on the range $370 \text{ nm} < \lambda < 610$ nm. The results are summarized in Fig. 5.2. The beam of 532 nm wavelength focuses at a distance of around ≈ 40 μm, while the 570 nm beam has the smallest width at a distance of around ≈ 70 μm behind the PhC. For the wavelength of 700 nm, which is already in the normal spatial dispersion regime according to the estimation above, no focusing was obtained.

Woodpile PhC samples, with the parameters used in the above FDTD calcula-

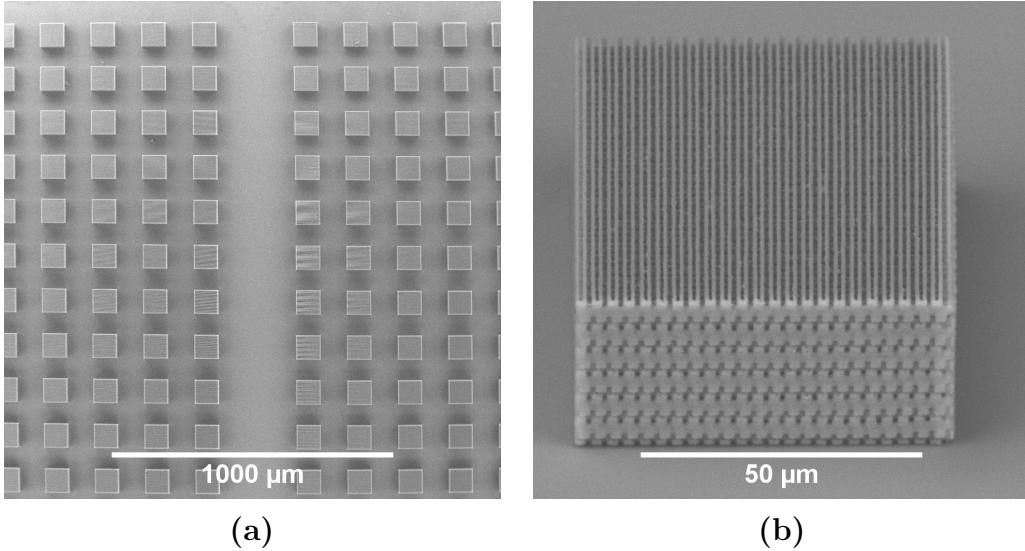


Fig. 5.3: Scanning electron micrographs of woodpile photonic crystals fabricated in hybrid photopolymer. (a) An example of array of crystals for parameter search; (b) the image of a woodpile crystal fabricated if optimum parameters.

tions, were fabricated by laser direct writing technique as described in 1 and 2 chapters of the Thesis. An example of PhCs, fabricated using optimum parameters is given in Fig. 5.3. For the experimental measurements a supercontinuum source pumped by an 800 nm Ti:sapphire laser was used. The particular wavelengths of 532, 570, and 700 nm were selected by a monochromator. The beams were focused using a $20\times$ NA 0.4 microscope objective onto the front face of the PhC, which for different frequencies resulted in waist widths varying from 1.6 to 3 μm. The beam profiles at different distances behind the crystal were recorded with a CCD camera mounted on a translational stage, together with the imaging system. The width of the beam behind the PhC was calculated, applying a Gaussian fit to the CCD images. The experimental results are summarized and compared with the FDTD calculation results in Fig. 5.2. Quantitative correspondence between the experimental and numerical data is not perfect, but the qualitative tendencies are the same.

The smallest beam diameter is found at particular distances (around 50 μm) behind the PhC at 532 and 570 nm, while monotonous spreading is observed at 700 nm. However, even in the latter case the divergence was slightly less than that of the reference beam, due to the spatial filtering of the beam (see next chapter). The minimum widths of the beam behind the PhC were around ≈ 2.1 μm and ≈ 3.4 μm at 570 and 532 nm, respectively. This result gives a rough estimation of the numerical aperture of the flat lens: $NA \approx 0.1$.

We note that we could not observe the beam focalization continuously throughout the expected wavelength range $\lambda_{BZ} < \lambda < \lambda_{SC}$, but just in several distinct areas of

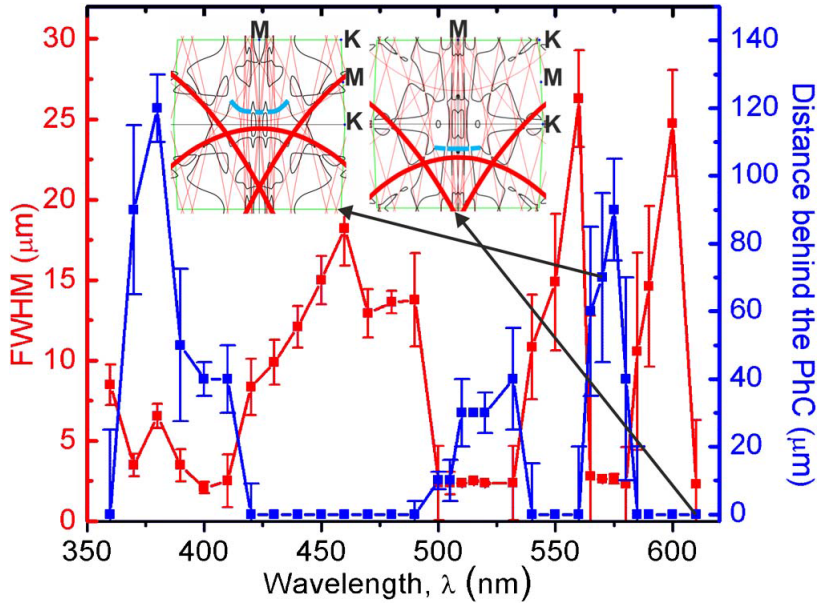


Fig. 5.4: Minimum diameter of the beam behind the PhC (red) and the focal distance (blue) versus wavelength calculated by FDTD. The two insets represent isofrequency lines, where the spanning harmonics (see main text) are highlighted in red and global trends of isofrequency are lines highlighted in blue. The left inset is at the frequency of flat lensing (at 570 nm) and the right one at self-collimation (at 610 nm).

this range. Figure 5.4 shows the focalization performance calculated by FDTD (the beam diameter at the focus as well the focal length depending on the wavelength). The reason for that is that we worked at very high-order propagation bands; although the character of the isofrequency lines is globally defined by the first harmonic of the index modulation, the higher harmonics interfere and distort the isoline picture. The higher the propagation band is, the more harmonics come into play, resulting in a stronger distortion of the isoline picture. As seen from Fig. 5.4 insets, although the isoline picture (calculated by the standard plane wave expansion method [62]) is quite disordered, the global trends can still be traced (highlighted in blue), indicating the appearance of flat segments (for SC) as well as positively curved segments (for flat lensing). The spanning harmonics are highlighted in red.

Conclusions

To conclude, we have reported the first (to our knowledge) experimental confirmation of beam focusing by a flat 3D woodpile PhC at visible frequencies. The results show a convincing flat lensing with focal distances of around $\approx 50 - 70 \mu\text{m}$ behind the crystal. No focusing appears at other wavelengths, excluding all possible refractive geometrical focusing effects (e.g., due to possibly curved surfaces of the woodpile). The observations are in good correspondence with the 2D FDTD simulations.

6

Control of spatial light spectrum by photonic crystals

¹ Spatial filtering is broadly used to improve the spatial quality of light beams. It allows to remove the unwanted frequency components from the spatial spectrum of waves. The constitution of the spatial spectrum is responsible for focusability, divergence and directionality of the beams, therefore in most of the applications it is important to have the highest quality beams, consisting of the lowest spatial frequencies. Spatial filtering is frequently used in laser systems, information processing, image enhancement, spatial spectrum analysis, improvement of directionality of antennas, etc [14, 68, 69].

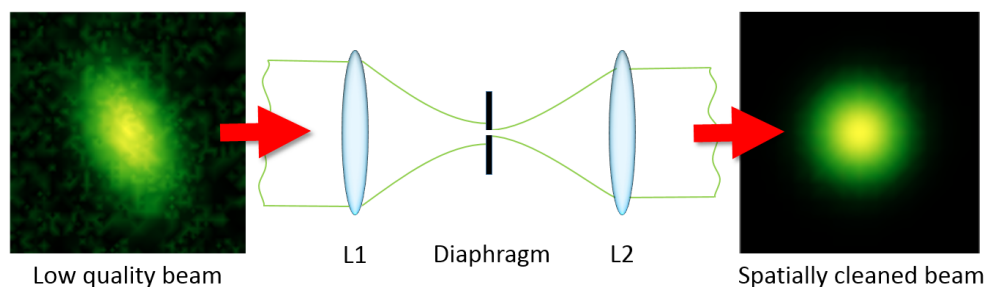


Fig. 6.1: Conventional spatial filtering technique uses a confocal system of lenses (L1, L2) to form a far field image in the focal plane, where a diaphragm of appropriate diameter is positioned in order to remove undesired angular components of the spatial spectrum.

A conventional technique of spatial filtering uses a confocal system of lenses to form a far field image in the focal plane, where a diaphragm of appropriate diameter is

¹This chapter of the Thesis is based on [A1], [A4], [A5], [A7] and ?? publications.

positioned in order to remove undesired angular components of the spatial spectrum (Fig. 6.1). However, such systems have some drawbacks: (1) they require the optical path of at least two focal lengths (typically 10 – 40 cm); (2) precise positioning of the diaphragm is needed; (3) they often suffer from mechanical instability; (4) it is difficult to fabricate focusing optics at some frequency ranges. Various alternative techniques have been suggested, which are based on the use of anisotropic media [70], resonant-grating systems [71, 72], interference patterns [73], multilayer stacks combined with a prism [51], and metallic grids [74], two-dimensional photonic crystals with [75] and without [53] defects, one-dimensional multilayer [76] and gradient PhCs [77].

Spatial filtering might be realized in three-dimensional photonic crystals by engineering the spatial dispersion $\omega(\vec{k})$ in such a way, that certain propagation directions are prohibited. In chapter 1.2 the two spatial filtering mechanisms were shown. The first and most obvious one is to implement the angular bandgaps, where no allowed states are present at certain directions. In this case, the unwanted radiation is reflected to the backward direction. Such type of filtering was proposed in 2D and 3D PhCs [14, 50, 51, 76]. In order to open the angular bandgaps the longitudinal periods must be shorter than the wavelength $d_{\parallel} < \lambda$. In visible range this corresponds to 200 – 400 nm periods which is still difficult to achieve with current technologies. This might be the reason why such filtering has never been shown in optics yet, although recently it was shown in acoustics [78, 79], where the longitudinal periods are of a few millimeters size and therefore are easier to fabricate.

Another way to achieve spatial filtering in 3D PhCs was proposed in [15]. In this case, the filtered out components are deflected to diffraction maxima. Such PhCs do not have the angular bandgaps. The longitudinal periods of these crystals might be several times larger, therefore such PhCs are much easier to fabricate. Such type of filtering was recently experimentally demonstrated in acoustics [78] and optics [80].

In this chapter of the Thesis several aspects of spatial filtering in PhCs are analyzed. Firstly, experimental spatial filtering by chirped PhCs is demonstrated followed by numerical simulations. Next, axisymmetric geometry of PhCs is proposed, which allows axisymmetric spatial filtering. Then, a super-collimation effect in axisymmetric PhCs is demonstrated.

PhCs for spatial light filtering applications were fabricated in a standard microscope soda-lime glass slides ($n \approx 1.52$) by a point-by-point modification of the refractive index using tightly focused femtosecond laser beam. Such direct laser writing technique is described more in detail in 1 and 2 chapters of the Thesis. For

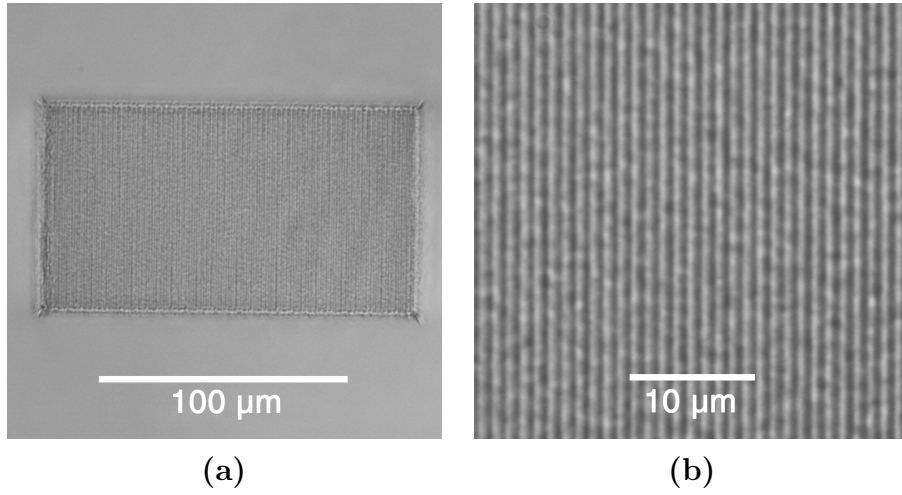


Fig. 6.2: The optical microscopy image view (a) and (b) the magnified image of the fabricated chirped structure.

characterization of filtering the PhC samples were illuminated by continuous 633 nm wavelength HeNe laser beam focused into PhC samples with 10× 0.3 NA objective. Focusing provides a large angular range of the radiation illuminating the PhC. By measuring the angular far field intensity profile at the output of the PhC one can determine which components are filtered out. To register the output a CCD camera was placed at 1-3 cm behind the sample (Fig. 6.2).

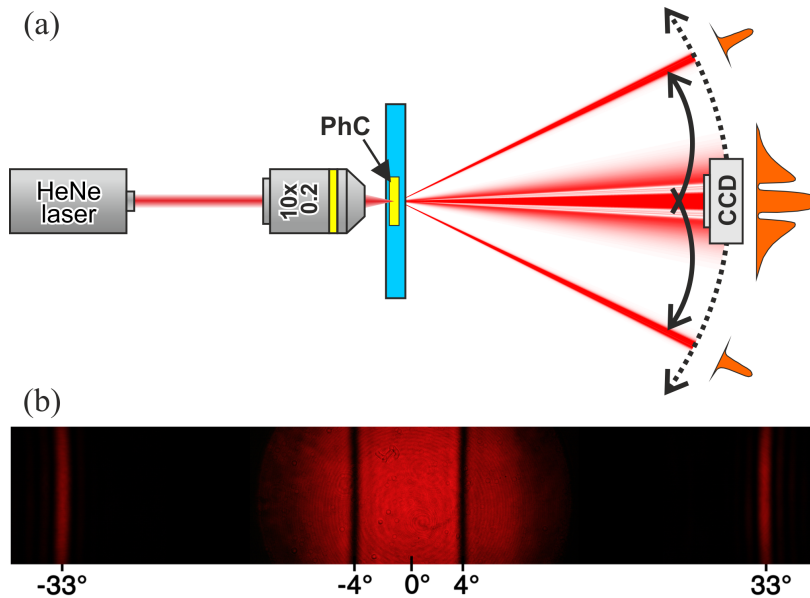


Fig. 6.3: Experimental measurement scheme (a): The HeNe laser beam is focused into PhC. Part of the angular components is deflected to the diffraction maxima and the rest passes through. A CCD camera placed on the rotational stage measures the angular intensity profiles. (b) A part of CCD camera image of the beam behind the PhC (far field image).

6.1 Spatial filtering by chirped photonic crystals

The fabrication of the gapless spatial filters is more convenient, as not so small longitudinal periods are required. On the other hand, the efficiency of filtering is restricted, as the deflected wave components propagate in forward direction, and can be scattered back into the modes of initial radiation. The process is summarized in Fig. 6.4, where the gapless filtering depending on the length of nonchirped PhC is shown.

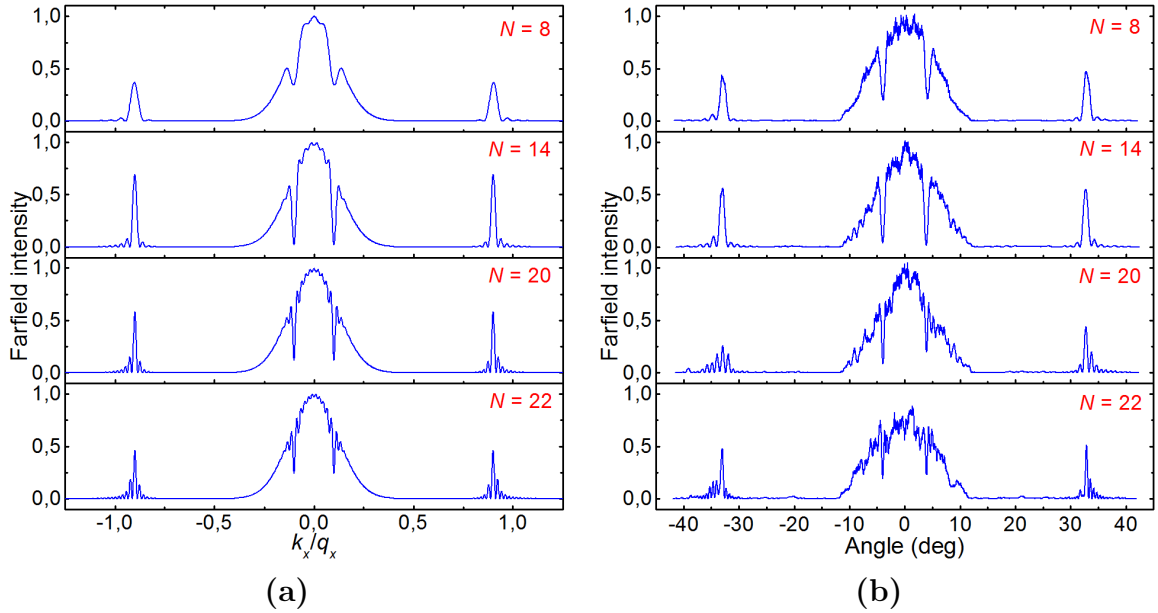


Fig. 6.4: Angular profiles of filtered radiation depending on the length of the non-chirped PhCs (in terms of number of periods N). (a) Numerical and (b) experimental results. Details are provided in the main text.

Evident is that initially the “dips” in the angular spectrum (the filtered out angular regions) increase in depth with increasing crystal length (Fig. 6.4, $N=8,14$). However, when the area being filtered is depleted to zero, the reverse process starts, and the efficiency of the filtering starts decreasing (Fig. 6.4, $N=20,22$). Moreover, the filtered out area appears to be not a smooth dip, but develops an oscillatory shape. This is in contrast with the spatial filtering based on the band gaps, where the filtered out radiation propagates in a backward direction, and cannot be scattered back. As a consequence, the filtered out angular areas monotonically increase with the propagation length in PhCs with angular band gaps.

In order to achieve efficient angular filtering the reverse scattering process is to be suppressed, i.e., the interaction between harmonics is to be allowed for a limited

propagation distance, and interrupted at the distance before the reverse process starts. For the parameters of Fig. 2, the optimum length providing maximum dip of filtered out components is approximately 14 periods. However, at the optimal distance the filtering dip is of a limited width. Another possibility to increase the efficiency is the use of chirped structures [15], where the longitudinal period varies along the photonic structure. As the filtering angle depends on the longitudinal period of the PhC, the angle sweeps along the chirped structure. As the result one can obtain simultaneously: (1) the angular range of filtered out components can be increased, i.e., determined by the sweep of the instantaneous filtering angle along the full length of the crystal; and (2) the reverse scattering process can be suppressed, as the efficient interaction length of the angular components is limited by the velocity of the sweep.

The section is devoted to the experimental demonstration of the above described idea, and to the quantitative analysis of the efficiency of the angular filtering in the presence of chirp.

The PhCs were designed to have 100 layers of parallel, equally spaced rods with a $1 \mu\text{m}$ transverse period. Every second layer was shifted by half of the transverse period with respect to the previous one, thus two layers result in one longitudinal period. For chirped crystals the longitudinal period d_{\parallel} is linearly incremented by Δd for every new period $d_{\parallel,i} = d_{\parallel,1} + i \cdot \Delta z$, where i counts the periods $i = 1, \dots, N$. The adimensional chirp parameter is defined by $C = \Delta z / \bar{d}_{\parallel}$, where $\bar{d}_{\parallel} = (d_{\parallel,1} + d_{\parallel,N})/2$ is the average distance between layers. We chose \bar{d}_{\parallel} to be $\bar{d}_{\parallel} = 6 \mu\text{m}$ and kept it constant in different samples, whereas the chirp parameter C was varied from sample to sample. Such fixed \bar{d}_{\parallel} corresponds to central filtering angle $\pm 4^\circ$.

The main results of the study are summarized in Fig. 6.5, which evidences the constructive role of the chirp for spatial filtering performance. The angular range as well as the energy of filtered-out radiation increases with increasing chirp as expected. The experimental results correspond qualitatively well to the numerical calculation results. Some discrepancy between the experimental measurements and numerical results appears, especially for large values of the chirp, which is due to imperfections of fabrication of the samples. Overall, although the measured efficiency of the filtering increases with increasing chirp parameter, the increase is, however, slower than that following from numerical calculations. Our interpretation is that for larger chirp parameters the filtered areas become more broad and “shallow” (for a fixed length of the sample) and generally they “collect” more noise due to the imperfections of

the structure. We note, however, that the detailed analysis of the randomness of structure requires separate analysis, and is beyond the scope of the present study.

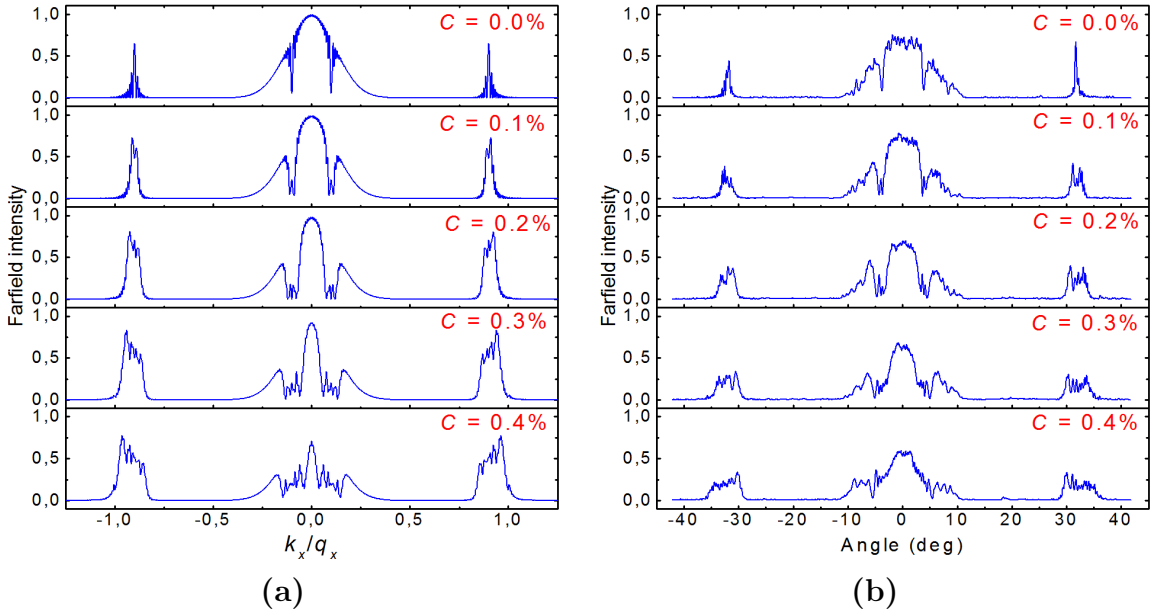


Fig. 6.5: Angular transmission profiles for varying chirp parameter C for PhC sample with $N = 50$ periods. (a) Numerical and (b) experimental results. Transverse wave number k_x is normalized to transverse wave number of refractive index modulation q_x in (a).

Next we calculate quantitative data of the filtering performance. We define filtering performance by

$$F = \frac{\int |\Delta I(k_{\perp})| dk_{\perp}}{\int |I(k_{\perp})| dk_{\perp}}, \quad (6.1)$$

which has a meaning of depletion of energy normalized to the full energy. The integration in (9) is performed over the Brillouin zone, i.e., on interval $k_{\perp} \in [-q_{\perp}/2, q_{\perp}/2]$. For proper geometry, when precisely the wings from the angular spectra are filtered out, the F is a measure of relative narrowing of the angular spectrum.

Figure 6.6(a) summarizes the dependence of the filtering performance on the chirp parameter. If the filtering in unchirped PhC structures of increasing length saturates for short crystals ($N=15$ periods), then for chirped crystals the saturation begins for longer crystals and results in higher filtering performance values, correspondingly. Figure 6.6(b) shows the dependence of filtering on the length of the sample for different chirp parameters C .

The above theoretical study is performed with the parameters corresponding to fabricated structures: The values of the coupling were $s = 0.05$ which correspond

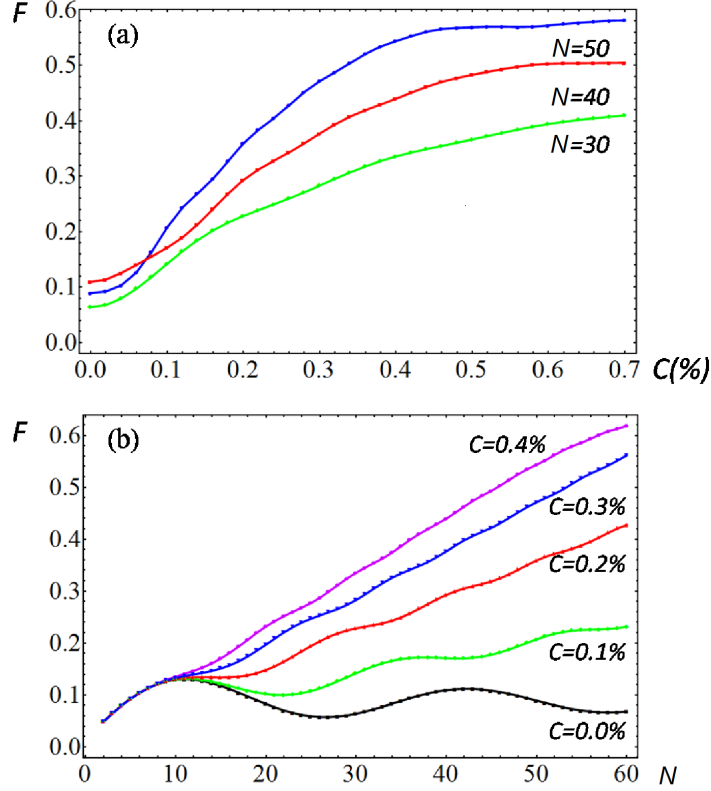


Fig. 6.6: Numerical study of the filtering performance: (a) dependences of filtering efficiency on chirp parameter for several crystals of different length (green plot for $N = 30$, red for $N = 40$, blue for $N = 50$); (b) Dependences of filtering efficiency on number of periods with different chirp parameters (black plot for $C = 0.0\%$; green for $C = 0.1\%$, red for $C = 0.2\%$, blue for $C = 0.3\%$, violet for $C = 0.4\%$).

to the maximum achievable coupling for structures imprinted in glass. We also restricted to realistic length of the PhC, possible to write without large distortions, which is approximately $N = 60$ periods. With the increasing length of the structure the imperfections of fabrication, as well as the losses and scattering of the structure, increase. However, even with these restrictions the filtering performance close to approximately 50% has been experimentally demonstrated. Looking into perspective, we analyzed the filtering performance of “hypothetical PhCs” with larger refraction index modulation, i.e., with corresponding larger coupling parameters s than those possible to obtain in reality for PhCs build in glasses. Examples of calculations for longer and higher index contrast photonic structures are shown in Fig. 6.7. Both calculated cases show that the filtering performance can reach the values of 80%, and could result in decreasing of the beam divergence by factor of 3. The filtering performance depending on parameters s , N , and C is summarized in Fig. 6.8. As follows from Figs. 6.8(a) and 6.8(c) the chirp parameter C has optimum values, which depend on the coupling parameter s : stronger coupling results in shorter filtering saturation length, therefore requires larger chirp for maximum filtering performances.

The dependence of filtering performance on the length of PhC, as follows from Figs. 6.8(b) and 6.8(d), shows the monotonic increase with eventual saturation.

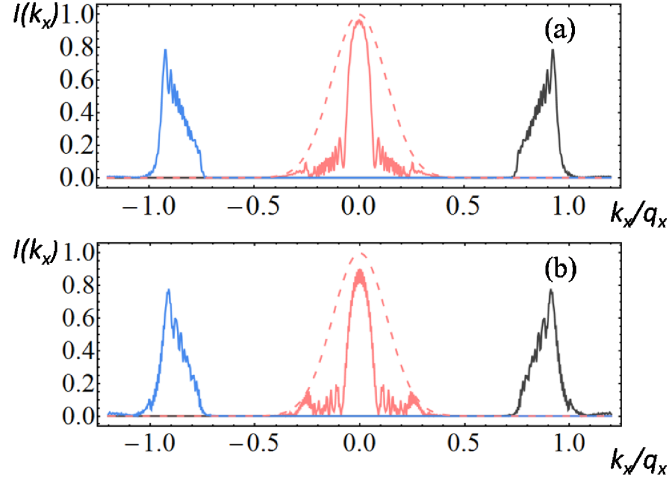


Fig. 6.7: Numerically obtained field profiles for spatial filtering in chirped structures with higher number of periods (a) and for higher refractive index contrast (b). The parameters for (a): $N = 120$, $s = 0.05$, $C = 0.24\%$, $d_{\parallel} = 7.44m$; for (b): $s = 0.1$, $N = 50$, $C = 0.53\%$, $d_{\parallel} = 7.2m$. The dashed line indicates angular profile of incident beam.

Conclusions

In conclusion, we have theoretically calculated and experimentally proved the effect of chirping of photonic crystal on the efficiency of spatial filtering. Our theoretical-numerical analysis reproduces well the experimental observations and interprets the observed effect as the spatial filtering in the gapless configuration. In spite of relatively weak index modulation (small scattering by one row) a substantial part of the radiation was shown to be filtered out. In order to obtain a technologically utile spatial filter the higher (but moderate) index contrast PhCs are necessary, which are to be based on new materials and fabrication technologies. A technologically relevant spatial filtering, allowing us to improve the beam quality parameter by the factor of 2–3, requires the refractive index modulation of order of approximately $\Delta n \approx 10^{-2}$.

Finally we highlight the advantage of the method of filtering demonstrated in this section. The main advantages (comparing with the conventional pinhole spatial filter) are: (1) extremely small thickness (hundreds of microns) of the filter enabling the integration of such a filter into micro-optical devices or into cavities of microlasers; (2)

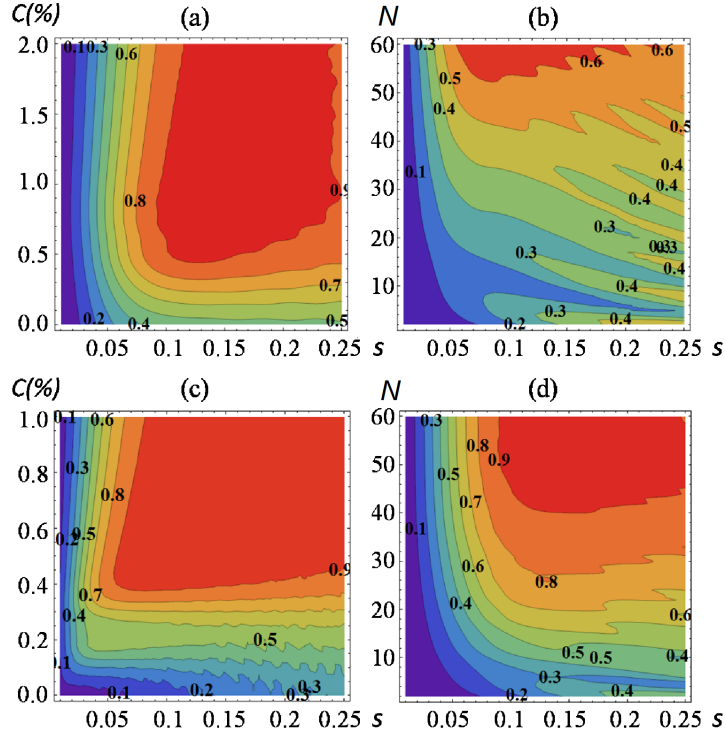


Fig. 6.8: The filtering efficiency, represented by isolines and by different colors, depending on sets of parameters. (a), (c) show dependencies on C and s ; (b), (d) show dependencies on N and s . Parameters: (a) $N = 50$, (c) $N = 120$. (b) $C = 0.3\%$, and (d) $C = 1\%$.

translational invariance of the PhC spatial filter (insensitivity to the lateral shift of PhC structure) simplifying its utilization; and (3) possibility to combine (to add) the filtering functionality to some other, already existing, functionalities (amplification, nonlinearities) in bulk material, by additional modulation of refraction index of the (amplifying or nonlinear) material.

6.2 Spatial filtering by axisymmetric photonic crystals

In section 6.1 the 1D spatial filtering was demonstrated, where 2D PhCs (with the modulation in longitudinal and in one transverse direction) were fabricated. The 1D filtering can be useful in specific applications, where the beam is distorted along only one transverse direction [see the illustration of 1D filtering in Fig. 6.9 (a, b)]. Most frequently, however, the 2D filtering is required in order to form axisymmetric beams of a high spatial quality. Generally speaking this should be performed by 3D PhC. The shape of the filtering window, however, depends strongly on the geometry of the 3D crystal. In particular, in [80] the filtering by 3D PhC with square symmetry in transversal plane has been demonstrated, which results in a square window of filtering, as shown in Fig. 6.9 (c, d). It is natural to expect that the

axisymmetric filtering requires an axisymmetric shape of the PhC (Fig. 6.9 (e, f)). A demonstration and analysis of such axisymmetric spatial filtering in axisymmetric PhCs is the subject of this section. First we provide numerical integrations of the light beam propagation through such a structure. Subsequently, based on the numerical calculation results we fabricate the crystal by femtosecond pulse writing in a bulk of glass and demonstrate the effect experimentally. In summary, among others, the scaling laws are discussed, enabling extension of the obtained results to different materials (different refractive index modulation amplitudes) and different practical needs (different angular resolutions of spatial filtering).

The layers of the axisymmetric microstructures were designed to have 100 concentric circles with $2\ \mu\text{m}$ separation between the rings in a layer. In every second layer the structure of rings was reciprocal; that is, the radii with refractive index maxima correspond to radii with index minima in the next layer. We chose the longitudinal period to be $\approx 13.4\ \mu\text{m}$. The chosen longitudinal period corresponds to a central filtering angle of $\approx 68\ \text{mrad}$, as follows from relation

$$\sin(\alpha) = \frac{q_{\perp}}{2|k_0|} (Q - 1) = \frac{\lambda}{2d_{\perp}} (Q - 1), \quad (6.2)$$

where $q_{\perp} = 2\pi/d_{\perp}$ is the transverse wavenumber of the index modulation, $k_0 = 2\pi/\lambda$ is the wavenumber of electromagnetic wave, $Q = \frac{2d_{\perp}^2 n}{\lambda d_{\parallel}}$ is the geometry factor, and n is the average refractive index. This equation indicates that the filtering angle α depends, among others, on the longitudinal period of modulation (through the parameter Q).

The experimentally recorded far field intensity distributions behind the axisymmetric filter are shown in Fig. 6.10. We clearly observe the appearance of a dark ring in the central part of the far field. For this particular geometry of photonic structure the radius of dark ring was $\approx 65\ \text{mrad}$, in correspondence with Eq. (6.2) ($69\ \text{mrad}$) derived in paraxial limit. The radiation from the dark ring is deflected to the bright ring (radius $396\ \text{mrad}$) consistent with the theory of diffraction of 1D grating. The increasing number of longitudinal periods of the structure leads to a more pronounced dark ring; that is, more energy is filtered to the outer bright ring.

Finally we performed a systematic study of the efficiency of the spatial filtering, depending on the crystal length (on the number of longitudinal periods). We estimated the width and depth of the filtering line and plotted its dependence on the crystal length in Fig. 6.11. As the profiles of the dark rings generally have irregular shape, the width of filtered rings was calculated as the distance between 10% and 90% intensity levels in integrated angular spectrum, using the well-established

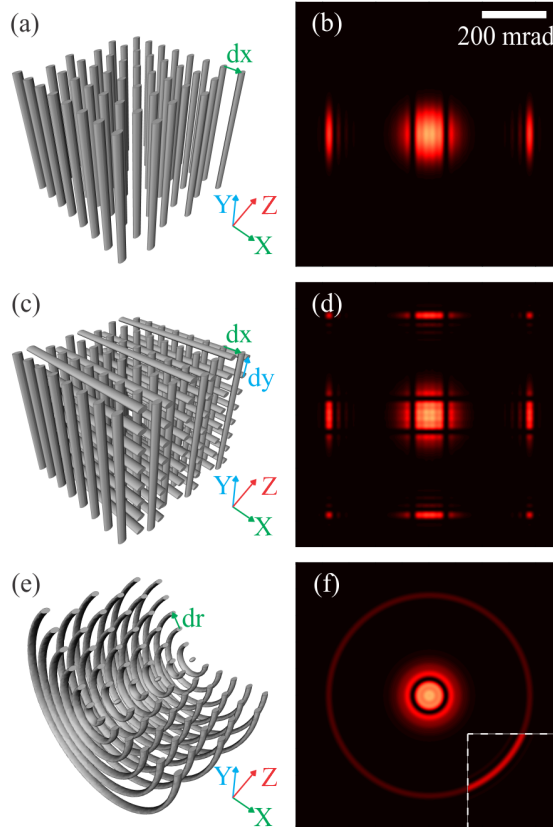


Fig. 6.9: (a), (c), and (e) Geometries of the photonic structures; and (b), (d), and (f) their far field distributions obtained by numerical calculations. (a) and (b) 2D case as considered in [10]; (c) and (d) square symmetry case in transverse plane case as considered in [9]; (e) and (f) spatial filtering in axisymmetric structures as considered in this Letter. The inset in (f) shows 5 times enhanced field intensity for visualization of the outer ring. The parameters for simulations are given in the main text.

knife edge method. We performed numerical calculations not only for the values corresponding to the fabricated structure $s = 0,15$ but also for smaller $s = 0,05$ and for larger $s = 0,25$ coupling coefficients, corresponding to the different amplitudes of index modulation.

According to Fig. 6.11, an optimum crystal length exists for a given amplitude of the refractive index modulation. The angular range of filtering decreases and the depth increases with increasing length of the structure, and the maximally narrow line is obtained, corresponding to nearly 100% filtering at the center of the angular filtering range. For longer structure the filtering line splits due to the back scattering (from outer (bright) ring to inner (dark) ring), typical of the gapless configuration and similar to 1D gapless filtering in the previous section.

The numerical analysis for the different amplitudes of refractive index modulation shows the perspective of the filtering for the PhC fabricated from crystals with the larger and smaller index contrast. In fact the simple analysis leads to the following scaling relations: the near 100% filtering is obtained under the condition $s \cdot N \approx 1.5$,

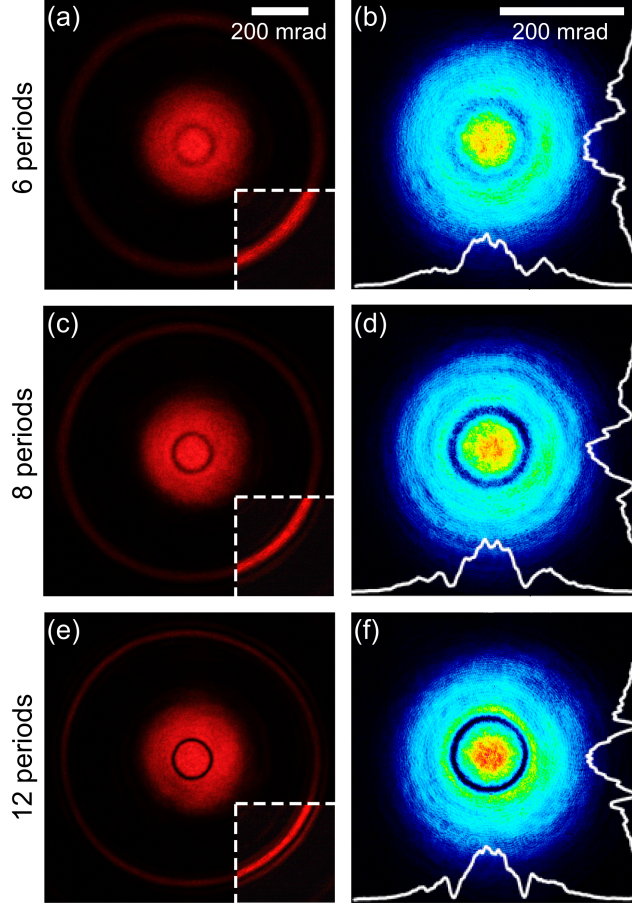


Fig. 6.10: Experimentally recorded far field distributions behind the axisymmetric structure for $N = 6, 8,$ and 12 longitudinal periods of the structure. (a), (c), and (e) show the large scale distributions; and (b), (d), and (f) show the small scale distributions together with their vertical cross sections through the axis of the beam. The radii of dark inner and light outer circles are 65 and 396 mrad, respectively. The insets in (b), (d), and (f) show 5 times enhanced field intensity for visualization of the bright

or equivalently $\Delta n \cdot l \approx 1.5$, where $l = d_{\parallel} \cdot N$ is the length of the structure and N is the number of longitudinal periods. The optimum width of the filtering line (which occurs at nearly 100% filtering at $s \cdot N \approx 1.5$) scales as $\phi_{min} \approx \Delta n$.

Conclusions

In conclusion, we have theoretically calculated and experimentally proved the axisymmetric spatial filtering in axisymmetric photonic microstructures (analogs of PhCs). Our theoretical-numerical analysis is in good correspondence with experimental observations.

Despite the fact that the refractive index modulation of the structure was relatively low, a substantial part of the radiation was filtered out. The angular range of the filtering line was around 25 mrad. This means that the spatial filters based on

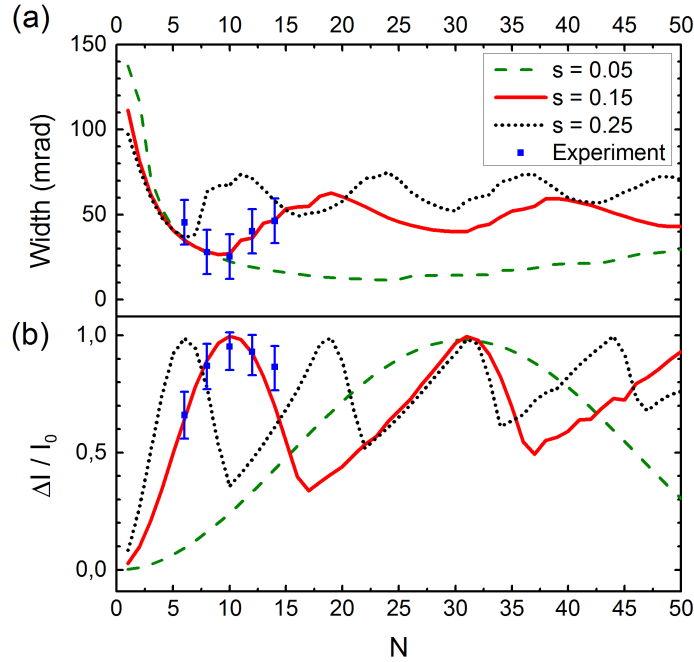


Fig. 6.11: (a) Numerically calculated width and (b) depth of the angular filtering range, depending on the length of the structure for three different s parameter values: 0.05, 0.15, and 0.25. The data from experimental measurements are shown by points with error bars. The red solid line corresponds to experimental values of s .

the fabricated structure could be used to substantially improve the spatial quality of the beams of around 50 mrad divergence.

The scaling discussed above suggests the materials and conditions for spatial filtering for different needs. In particular, to improve the spatial quality of beams in solid-state lasers, where the typical divergence is several mrad, the amplitude of refractive index must be on the order of 10^{-3} . The structures, however, must be relatively long ($N \approx 80$ periods) to provide the near 100% filtering. On the contrary, to improve the beam structure of semiconductor microlasers with typical divergence of the beams of approximately >100 mrad, the amplitude of refractive index modulations must be on the order of $\Delta n \approx 0,1$. The latter is hardly possible using inorganic glasses but presumably can be done in polymers [81] or dichromated gelatin films [82, 83].

Finally, we comment on the advantages of the method of spatial filtering shown in this section (compared with the conventional spatial filter with confocal arrangement of lenses): (1) the extremely small thickness (hundreds of microns), which enables integration of such a filter into micro-optical devices or into cavities of microlasers; and (2) the possibility of combining (adding) the filtering functionality to other functionalities (amplification, nonlinearities) in bulk material, by additional modulation of the refractive index of the (amplifying or nonlinear) material. One more advantage of 1D spatial filters, which is the translational invariance of the PhC

spatial filter (insensitivity to the lateral shift of PhC structure), is, however, lost in 2D axisymmetric spatial filters due to the presence of the optical axis.

6.3 Supercollimation effect in axisymmetric photonic crystals

It is known that Photonic Crystals (PhCs) can display exotic wave propagation properties such as anomalous refraction and diffraction of Bloch modes [44, 46]. Flat PhC lensing is perhaps a best known realisation of anomalous diffraction/refraction, which has been recently demonstrated in conventional [45] and sub-wavelength [65] resolution. The wave propagation principles in flat PhC lensing are similar to those in metamaterials with negative refraction [12, 84]. These flat lensing effects [45, 65], also flat mirror focusing effects [85, 86], are the near field phenomena, as the flat, transversally invariant PhC lenses and mirrors do not affect the far field distributions of the transmitted radiation. The beam manipulation with PhCs in the far field domain get less attention: perhaps the only known effect of PhC action on the spatial frequency spectrum is a spatial (angular) filtering of the beams due to the angular band-gaps [14, 76, 80].

In spatial filtering, a range of the angular components of a beam can be removed due to the angular band-gaps, i.e., the waves can be reflected in backward direction [14, 76] or deflected at large angles in forward direction [15]. In the latter case, the angular distribution of the transmitted field is modified as illustrated in Fig. 6.12(a). Some angular components of transmitted field can be attenuated (see the formation of dips in Fig. 6.12(a), however, obviously, no angular components can be amplified.

In this section an unexpected phenomenon observed in axisymmetric PhCs is reported, where the on- or around-axis field components are strongly amplified. The structure which we consider consists of the periodic planes of concentric rings, as illustrated in Fig. 6.12(b). The axisymmetric deflection of the angular components is possible, resulting in axisymmetric angular filtering, similarly to the spatial filtering in conventional periodic PhCs. However, unexpectedly, near-axis field components of transmitted radiation were observed to increase strongly, and an intense bright peak was observed in the far field of the transmitted radiation, as shown in Fig. 6.12(b). This, as discussed in detail further on, occurs for a precise matching between the longitudinal and transverse periods of the axisymmetric PhC. This enhancement of the field in the central area of the far field distribution, as detailed below, was measured experimentally up to 7 times in terms of intensity. The output of the experiment was a well collimated beam, with the divergence of approximately 20 mrad. The report and interpretation of the effect are the main message of this

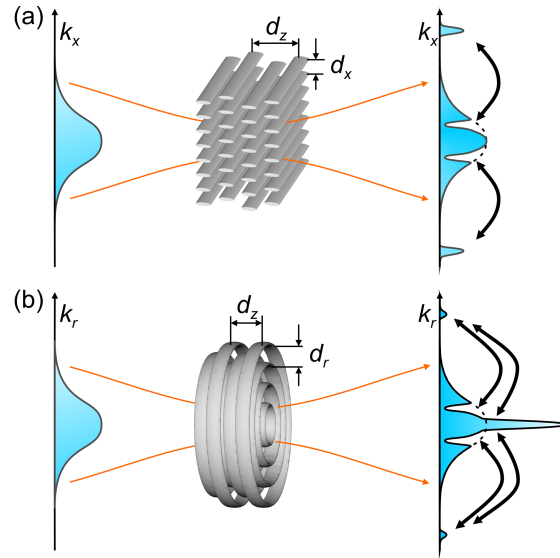


Fig. 6.12: Illustration of the spatial filtering in: (a) periodic two-dimensional PhC (periodic array of parallel rods) and (b) and in axisymmetric PhC. Dashed lines indicate the far field profile without the structure. Arrows indicate diffractive scattering of the field components in forward direction (angular filtering), and in backward direction.

section.

Before moving to the details, we note that the phenomenon is possible only in the case of axisymmetric PhCs. No enhancement in far field can be achieved in purely periodic conventional PhCs, two-dimensional or three-dimensional, what follows from experimental and numerical studies, and also from plane-wave expansion analysis. This means that Bloch modes propagating in different directions (corresponding to different angular components) are uncoupled in conventional PhCs. The effect is based on a diffusive mixing of different radial wave-components in axisymmetric PhCs.

The layers of the axisymmetric microstructures were designed to contain 30 concentric circles at $2\ \mu\text{m}$ increment of radii of rings in a layer. In every second layer, the structure of rings is reciprocal, i.e., the radii with refractive index maxima correspond to radii with index minima in the next layer (next longitudinal half-period). The longitudinal period of the structure was calculated according to Eq. (6.2). In order to achieve optimum super-collimation effect, we work in the range of small filtering angles ($\alpha \approx 0$); therefore, the longitudinal period according to Eq. (6.2) was varied around the value $d_{\parallel} \approx 19\ \mu\text{m}$ for the 633 nm wavelength of HeNe laser.

The key experimental observation results are summarized in Fig. 6.13. The laser beam was focused just in front of the PhC sample with a 0.3 NA objective. The beam half-width at waist was $2\ \mu\text{m}$, which corresponded to angular divergence of 180 mrad. We recorded the far field profiles of the beam by CCD camera positioned

at approximately 10 mm distance behind the sample. Figs. 6.13(a) and 6.13(b) show the far field distributions (together with their axial cross-sections taken at each 45° angle) at optimum geometry for the super-collimation. The far-fields at different propagation lengths (different lengths of the structure in experiments) show the formation of the super-collimated beam. For comparison, the beam propagation in PhC with a geometry designed for spatial filtering (Fig. 6.13(c)) shows no super-collimation effects (for the identical fabrication conditions of the structure, except for the different longitudinal periods, i.e., different geometry parameters and lower number of periods $N = 12$). The latter distribution shows spatial filtering, similarly to that reported in previous section for this geometry, but no super-collimation.

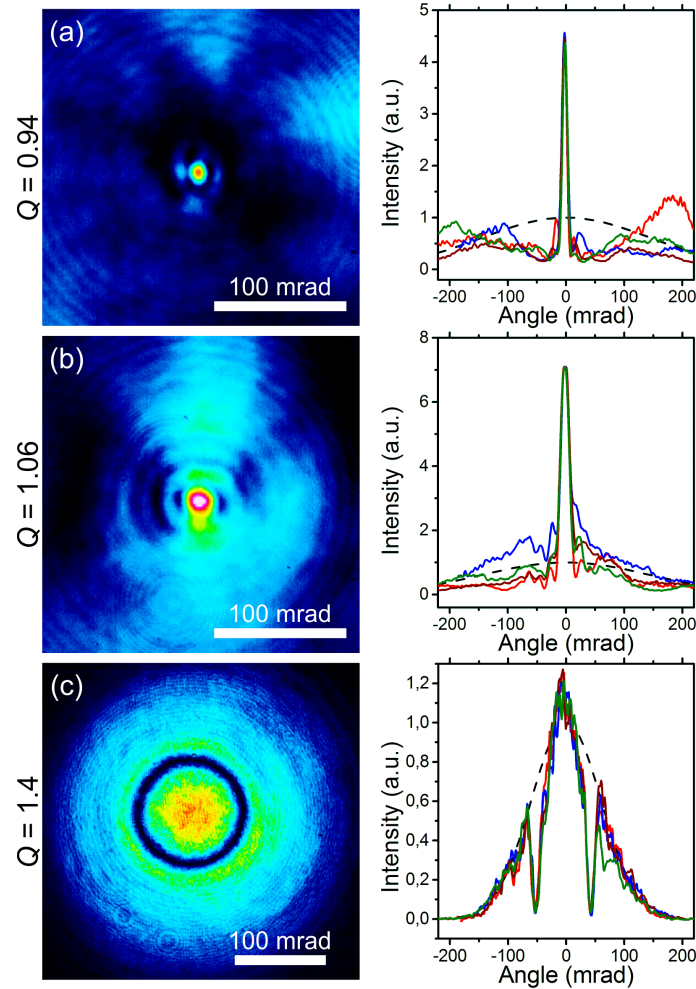


Fig. 6.13: The 2D far field intensity profiles together with their axial (vertical, horizontal, and both diagonal) cross-sections for the parameters corresponding to super-collimation (a) and (b), and deviated from the self-collimation regime (c). (a) and (b) contains $N = 20$ periods of $d_{\parallel} = 20.4 \mu\text{m}$ and $d_{\parallel} = 18.1 \mu\text{m}$, respectively, and (c) has $N = 12$ periods of $d_{\parallel} = 13.7 \mu\text{m}$.

The detailed mechanism for super-collimation remains unclear. Evident is that the effect is related with axisymmetric diffusion in far field domain, i.e., with inter-mixing of different radial field components, as also schematically illustrated in Fig. 6.12.

Let us consider first the perfectly periodic PhC, with transverse period d_{\perp} ($q_{\perp} = 2\pi/d_{\perp}$), see Fig. 6.12(a). Then the arbitrary plane wave component with transverse k_{\perp} ($k_0^2 = k_{\perp}^2 + k_{\parallel}^2$) can be scattered into $k_{\perp} + q_{\perp}m$ ($m = \pm 1, \pm 2, \dots$). The set of coupled plane waves with given k_{\perp} builds the Bloch mode propagating invariantly along the modulated structure. Important is that different Bloch modes (the ones with different k_{\perp} 's), being orthogonal, do not couple in between in propagation, i.e., propagate independently one from another. The character of the Bloch mode depends also on the longitudinal period: at the resonance condition, the coupling between the plane wave components building the Bloch mode is strong, so the angular filtering is obtained for particular range of k_{\perp} (the angular range). In this way, different angular field components do not mix, i.e., the excitations do not diffuse across the angular spectrum in periodic structures. In axisymmetric structures, however, the backward diffraction does not bring the radiation back to initial k_{\perp} , but, to a particular range of $k_{\perp} \pm \Delta k_{\perp}$, which results in a kind of diffusion in far field domain.

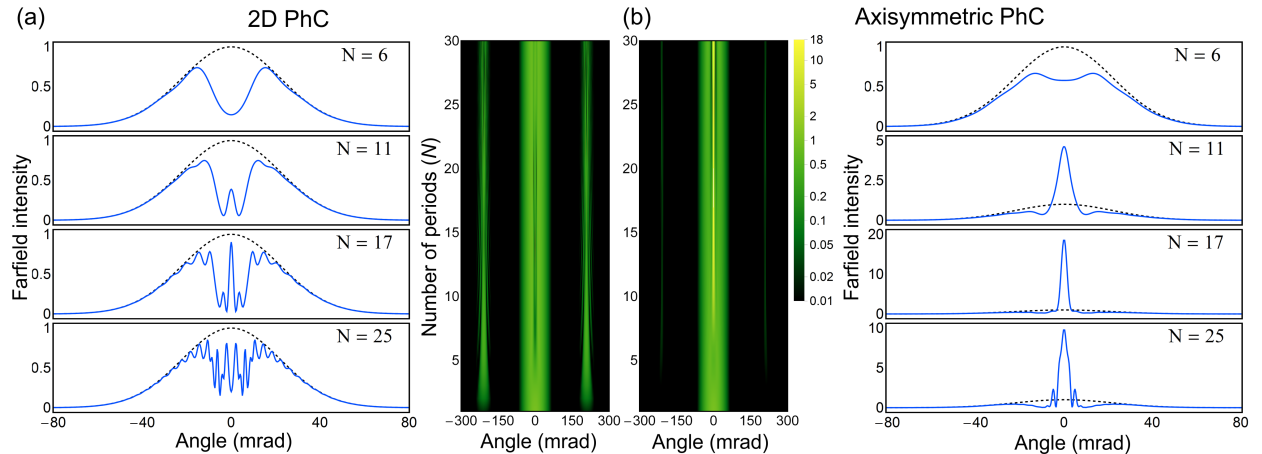


Fig. 6.14: Comparison of the spatial filtering in conventional 2D PhC, and in axisymmetric PhC. The far field angular distributions (blue solid lines) at indicated propagated distances N (in periods), as well as the 2D maps attribute to (a) 2D PhC and (b) axisymmetric PhC. Dashed lines represent the far field intensity profiles of the unity normalized Gaussian input beam.

This interpretation has been checked by a series of numerical calculations. The coupling coefficient of one layer was estimated from the above expression $s \approx 0.15$,

which means that approximately $\approx 2\%$ of radiation energy is deflected by each layer. This estimation was checked *a posteriori* comparing the experimental results with the results of numerical analysis with varied coupling coefficient s . The above interpretation of the super-collimation is supported by numerical calculations of the beam propagation along the structure, presented in Fig. 6.14. On the left side, the wave propagation along the 2D PhC is shown proving the well-established theory that the Bloch modes do not couple. The dips appear according to the angular filtering theory at the optimum propagation distance, and are afterwards filled back due to back-scattering for longer than optimum propagation distance. On the right side of Fig. 6.14, for axisymmetric structures, the initial formation of the dip (the forward scattering) is similar to that in conventional 2D PhCs. The back-scattering process, however, results in a kind of diffusion, i.e., the mixing of the angular wave-components, and eventually to the formation of the super-collimation.

The effect of super-collimation, as can be expected, depends strongly on the geometric parameters. Fig. 6.15 summarizes that dependence: the maximum-intensity of the super-collimated beam has been plotted in 2D parameter space of (geometry parameter Q , length in periods N). The area of optimum super-collimation is clearly seen at around $Q \approx 1$. In fact, this area is split into two, one for $Q < 1$ and one for $Q > 1$. The experimental results in Fig. 6.13 are obtained for the parameters approximately corresponding to these two peaks. Note that the numerical map was calculated for a fixed s and for fixed width of the beam. From the study also follows that the length of the structure has an optimum. Longer than optimal structures do not improve, but rather diminish the super-collimation.

Conclusions

In conclusion, we have predicted and experimentally demonstrated the super-collimation effect in axisymmetric photonic structures. We interpret the effect in terms of radial diffusion of the radiation in the far field domain, during the forward-backward diffractive scattering cascade. In our experiments, the maximum enhancement of the intensity of around 7 times was recorded, and the angular distribution of super-collimated beam of around 20 mrad was observed. In the numerical studies, we observed even larger >20 times enhancement of the intensity, where around 30% of energy was within the super-collimated beam. The experimental deviation from numerical results is most likely caused by spherical aberrations during fabrication process, which decreased the quality of our rather long ($\approx 350 \mu\text{m}$ height) structures. Such aberrations could, in principle, be compensated with spatial light modulator

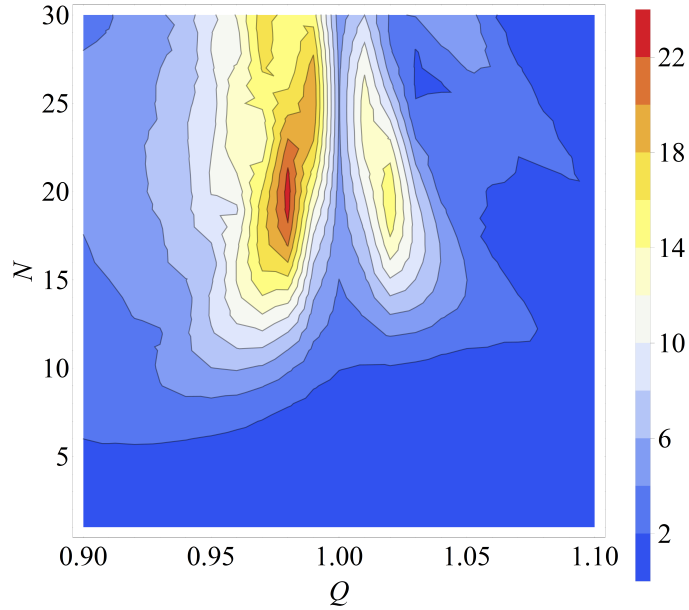


Fig. 6.15: Map of on-axis intensity enhancement in the parameter plane of (Q, N) , showing the optimum geometry and the optimum length (in periods) of the structure.

[87, 88] or other techniques. We note that the effect of super-collimation weakly depends on the position of focusing in front (or behind) the crystal. The position could be changed by $\approx \pm 0.5$ mm without a substantial influence on super-collimation. In usual (or in Fresnel) lensing, the divergence of the collimated beam would be very sensitive to the position of the focus (of source) along the axis. Finally, we note that the demonstrated effect could be well utilized outside the optics, in other fields of wave dynamics. Recently, the spatial filtering has been shown for acoustic beams[78, 79] – the idea we promote might be well utilized for the formation of super-collimated beams in acoustics too.

Reference list

- [1] J. W. Strutt (Lord Rayleigh), On the Maintenance of Vibrations by Forces of Double Frequency, and on the Propagation of Waves Through a Medium Endowed with a Periodic Structure, *Philos. Mag.* **24**(147), 145–159 (1887)
- [2] J. W. Strutt (Lord Rayleigh), On the Remarkable Phenomenon of Crystalline Reflexion described by Professor Stokes, *Philos. Mag.* **26**(160), 256–65 (1888)
- [3] E. Yablonovitch, Inhibited Spontaneous Emission in Solid-State Physics and Electronics, *Phys. Rev. Lett.* **58**(20), 2059–2062 (1987)
- [4] S. John, Strong localization of photons in certain disordered dielectric superlattices, *Phys. Rev. Lett.* **58**(23), 2486–2489 (1987)
- [5] Z. Lu, S. Shi, J. Murakowski, G. Schneider, C. Schuetz, and D. Prather, Experimental Demonstration of Self-Collimation inside a Three-Dimensional Photonic Crystal, *Phys. Rev. Lett.* **96**(17), 173902 (2006)
- [6] V. Espinosa, V. Sanchez-Morcillo, K. Staliunas, I. Perez-Arjona, and J. Redondo, Subdiffractive propagation of ultrasound in sonic crystals, *Phys. Rev. B* **76**(14), 140302(R) (2007)
- [7] J. Witzens, M. Loncar, and A. Scherer, Self-collimation in planar photonic crystals, *IEEE J. Sel. Top. Quant. Electron.* **8**(6), 1246–1257 (2002)
- [8] I. Perez-Arjona, V. Sanchez-Morcillo, J. Redondo, V. Espinosa, and K. Staliunas, Theoretical prediction of the nondiffractive propagation of sonic waves through periodic acoustic media, *Phys. Rev. B* **75**(1), 014304 (2007)
- [9] D. Tang, L. Chen, and W. Ding, Efficient beaming from photonic crystal waveguides via self-collimation effect, *Appl. Phys. Lett.* **89**(13), 131120 (2006)
- [10] H. Kosaka, T. Kawashima, A. Tomita, M. Notomi, T. Tamamura, T. Sato, and S. Kawakami, Self-collimating phenomena in photonic crystals, *Appl. Phys. Lett.* **74**(9), 1212 (1999)
- [11] M. Notomi, Negative refraction in photonic crystals, *Opt. Quantum. Electron.* **34**(1/3), 133–143 (2002), URL <http://dx.doi.org/10.1023/A:1013300825612>
- [12] J. B. Pendry, Negative Refraction Makes a Perfect Lens, *Phys. Rev. Lett.* **85**(18), 3966–3969 (2000)
- [13] G. W. Milton, N.-A. P. Nicorovici, R. C. McPhedran, and V. A. Podolskiy, A proof of superlensing in the quasistatic regime, and limitations of superlenses in this regime due to anomalous localized resonance, *Proc. R. Soc. A* **461**(2064), 3999–4034 (2005)
- [14] E. Colak, A. O. Cakmak, A. E. Serebryannikov, and E. Ozbay, Spatial filtering using dielectric photonic crystals at beam-type excitation, *J. Appl. Phys.*

-
- 108**(11), 113106 (2010)
- [15] K. Staliunas and V. Sanchez-Morcillo, Spatial filtering of light by chirped photonic crystals, *Phys. Rev. A* **79**(5), 053807 (2009)
- [16] T. Baba, Slow light in photonic crystals, *Nature Photon* **2**(8), 465–473 (2008)
- [17] P. Russell, Photonic crystal fibers, *Science* **299**(5605), 358–362 (2003)
- [18] A. D. Pris, Y. Utturkar, C. Surman, W. G. Morris, A. Vert, S. Zalyubovskiy, T. Deng, H. T. Ghiradella, and R. A. Potyralo, Towards high-speed imaging of infrared photons with bio-inspired nanoarchitectures, *Nature Photon* **6**(3), 195–200 (2012)
- [19] E. Yablonovitch, T. Gmitter, and K. Leung, Photonic band structure: The face-centered-cubic case employing nonspherical atoms, *Phys. Rev. Lett.* **67**(17), 2295–2298 (1991)
- [20] S. Y. Lin, J. G. Fleming, D. L. Hetherington, B. K. Smith, R. Biswas, K. M. Ho, M. M. Sigalas, W. Zubrzycki, S. R. Kurtz, and J. Bur, A three-dimensional photonic crystal operating at infrared wavelengths, *Nature* **394**(6690), 251–253 (1998)
- [21] M. E. McNamara, D. E. G. Briggs, P. J. Orr, S. Wedmann, H. Noh, and H. Cao, Fossilized biophotonic nanostructures reveal the original colors of 47-million-year-old moths, *PLoS Biol.* **9**(11), e1001200 (2011)
- [22] M. Srinivasarao, Nano-Optics in the Biological World: Beetles, Butterflies, Birds, and Moths, *Chem. Rev.* **99**(7), 1935–1962 (1999)
- [23] A. Saito, Material design and structural color inspired by biomimetic approach, *Sci. Technol. Adv. Mater.* **12**(6), 064709 (2011)
- [24] S. Kinoshita and S. Yoshioka, Structural Colors in Nature: The Role of Regularity and Irregularity in the Structure, *ChemPhysChem* **6**(8), 1442–1459 (2005)
- [25] S. Kinoshita, S. Yoshioka, Y. Fujii, and N. Okamoto, Photophysics of Structural Color in the Morpho Butterflies, *Forma* **17**(2), 103–121 (2002)
- [26] S. Kinoshita, S. Yoshioka, and J. Miyazaki, Physics of structural colors, *Reports on Progress in Physics* **71**(7), 076401 (2008)
- [27] X. Gao, X. Yan, X. Yao, L. Xu, K. Zhang, J. Zhang, B. Yang, and L. Jiang, The Dry-Style Antifogging Properties of Mosquito Compound Eyes and Artificial Analogues Prepared by Soft Lithography, *Adv. Mater.* **19**(17), 2213–2217 (2007)
- [28] P. Vukusic and J. R. Sambles, Photonic structures in biology., *Nature* **424**(6950), 852–855 (2003)
- [29] J. W. Galusha, L. R. Richey, J. S. Gardner, J. N. Cha, and M. H. Bartl, Discovery of a diamond-based photonic crystal structure in beetle scales, *Phys. Rev. E* **77**(5), 050904 (2008)
- [30] Y. Zhao, Z. Xie, H. Gu, C. Zhu, and Z. Gu, Bio-inspired variable structural color materials, *Chem. Soc. Rev.* **41**(8), 3297 (2012)
- [31] S. G. Johnson and J. D. Joannopoulos, Three-dimensionally periodic dielectric layered structure with omnidirectional photonic band gap, *Appl. Phys. Lett.*

- 77**(22), 3490 (2000)
- [32] R. A. Potyrailo, H. Ghiradella, A. Vertiatchikh, K. Dovidenko, J. R. Cournoyer, and E. Olson, Morpho butterfly wing scales demonstrate highly selective vapour response, *Nature Photon* **1**(2), 123–128 (2007)
- [33] K. Chung, S. Yu, C.-J. Heo, J. W. Shim, S.-M. Yang, M. G. Han, H.-S. Lee, Y. Jin, S. Y. Lee, N. Park, and et al., Flexible, Angle-Independent, Structural Color Reflectors Inspired by Morpho Butterfly Wings, *Adv. Mater.* **24**(18), 2375–2379 (2012)
- [34] H. Wang and K.-Q. Zhang, Photonic Crystal Structures with Tunable Structure Color as Colorimetric Sensors, *Sensors* **13**(4), 4192–4213 (2013)
- [35] O. Zitouni, K. Boujdaria, and H. Bouchriha, Band parameters for GaAs and Si in the 24-k.p model, *Semicond. Sci. Technol.* **20**(9), 908–911 (2005)
- [36] J. D. Joannopoulos, S. G. Johnson, J. N. Winn, and R. D. Meade, *Photonic Crystals: Molding the Flow of Light* (Second Edition), (Princeton University Press, Princeton, 2008)
- [37] L. V. Hau, S. E. Harris, Z. Dutton, and C. H. Behroozi, Light speed reduction to 17 metres per second in an ultracold atomic gas, *Nature* **397**(6720), 594–598 (1999)
- [38] L. V. Hau, Optical information processing in Bose–Einstein condensates, *Nature Photon* **2**(8), 451–453 (2008)
- [39] S. Residori, U. Bortolozzo, and J. Huignard, Slow and Fast Light in Liquid Crystal Light Valves, *Phys. Rev. Lett.* **100**(20), 203603 (2008)
- [40] T. F. Krauss, Slow light in photonic crystal waveguides, *J. Phys. D: Appl. Phys.* **40**(9), 2666–2670 (2007)
- [41] M. Notomi, Manipulating light with strongly modulated photonic crystals, *Reports on Progress in Physics* **73**(9), 096501 (2010)
- [42] S. Johnson, P. Bienstman, M. Skorobogatiy, M. Ibanescu, E. Lidorikis, and J. Joannopoulos, Adiabatic theorem and continuous coupled-mode theory for efficient taper transitions in photonic crystals, *Phys. Rev. E* **66**(6), 066608 (2002)
- [43] M. Notomi, Theory of light propagation in strongly modulated photonic crystals: Refractionlike behavior in the vicinity of the photonic band gap, *Phys. Rev. B* **62**(16), 10696–10705 (2000)
- [44] C. Luo, S. Johnson, J. Joannopoulos, and J. Pendry, All-angle negative refraction without negative effective index, *Phys. Rev. B* **65**(20) (2002)
- [45] P. V. Parimi, W. T. Lu, P. Vodo, and S. Sridhar, Photonic crystals: Imaging by flat lens using negative refraction, *Nature* **426**(6965), 404–404 (2003)
- [46] E. Cubukcu, K. Aydin, E. Ozbay, S. Foteinopoulou, and C. M. Soukoulis, Electromagnetic waves: Negative refraction by photonic crystals, *Nature* **423**(6940), 604–605 (2003)
- [47] Z. Lu, C. Chen, C. A. Schuetz, S. Shi, J. A. Murakowski, G. J. Schneider, and D. W. Prather, Subwavelength imaging by a flat cylindrical lens using optimized

-
- negative refraction, *Appl. Phys. Lett.* **87**(9), 091907 (2005)
- [48] Z. Lu, J. Murakowski, C. Schuetz, S. Shi, G. Schneider, and D. Prather, Three-Dimensional Subwavelength Imaging by a Photonic-Crystal Flat Lens Using Negative Refraction at Microwave Frequencies, *Phys. Rev. Lett.* **95**(15), 153901 (2005)
- [49] H. Kosaka, T. Kawashima, A. Tomita, M. Notomi, T. Tamamura, T. Sato, and S. Kawakami, Superprism phenomena in photonic crystals, *Phys. Rev. B* **58**(16), R10096–R10099 (1998)
- [50] Z. Tang, D. Fan, S. Wen, and C. Zhao, Low-pass spatial filtering using a two-dimensional self-collimating photonic crystal, *Chinese Optics Letters* **5**, 211–213 (2007)
- [51] I. Moreno, J. J. Araiza, and M. Avendano-Alejo, Thin-film spatial filters, *Opt. Lett.* **30**(8), 914–916 (2005)
- [52] Z. Tang, H. Zhang, Y. Ye, C. Zhao, S. Wen, and D. Fan, Low-pass Spatial Filtering Using Optically Thinner Left-handed Photonic Crystals, 2006 International Symposium on Biophotonics, Nanophotonics and Metamaterials 488–491 (2006)
- [53] A. E. Serebryannikov, A. Y. Petrov, and E. Ozbay, Toward photonic crystal based spatial filters with wide angle ranges of total transmission, *Appl. Phys. Lett.* **94**(18), 181101 (2009)
- [54] T. H. Maiman, Stimulated Optical Radiation in Ruby, *Nature* **187**(4736), 493–494 (1960)
- [55] R. R. Gattass and E. Mazur, Wiring light with femtosecond laser pulses, *Photonics Spectra* **12**, 56–60 (2004)
- [56] K. M. Davis, K. Miura, N. Sugimoto, and K. Hirao, Writing waveguides in glass with a femtosecond laser, *Opt. Lett.* **21**(21), 1729 (1996)
- [57] S. Maruo, O. Nakamura, and S. Kawata, Three-dimensional microfabrication with two-photon-absorbed photopolymerization, *Opt. Lett.* **22**(2), 132–134 (1997)
- [58] E. Yablonovitch and T. Gmitter, Photonic band structure: The face-centered-cubic case, *Phys. Rev. Lett.* **63**(18), 1950–1953 (1989)
- [59] J. Fischer and M. Wegener, Three-dimensional optical laser lithography beyond the diffraction limit, *Laser & Photonics Reviews* **7**(1), 22–44 (2013)
- [60] V. Mizeikis, K. K. Seet, S. Juodkazis, and H. Misawa, Three-dimensional woodpile photonic crystal templates for the infrared spectral range, *Opt. Lett.* **29**(17), 2061–2063 (2004)
- [61] M. Straub, M. Ventura, and M. Gu, Multiple Higher-Order Stop Gaps in Infrared Polymer Photonic Crystals, *Phys. Rev. Lett.* **91**(4), 043901 (2003)
- [62] S. Johnson and J. Joannopoulos, Block-iterative frequency-domain methods for Maxwells equations in a planewave basis, *Opt. Express* **8**(3), 173 (2001)
- [63] A. Ovsianikov, X. Shizhou, M. Farsari, M. Vamvakaki, C. Fotakis, and B. N. Chichkov, Shrinkage of microstructures produced by two-photon polymerization of Zr-based hybrid photosensitive materials., *Opt. Express* **17**(4), 2143–2148

- (2009)
- [64] J. Serbin and M. Gu, Superprism phenomena in waveguide-coupled woodpile structures fabricated by two-photon polymerization, *Opt. Express* **14**(8), 3563–3568 (2006)
 - [65] E. Cubukcu, K. Aydin, E. Ozbay, S. Foteinopoulou, and C. Soukoulis, Subwavelength Resolution in a Two-Dimensional Photonic-Crystal-Based Superlens, *Phys. Rev. Lett.* **91**(20), 207401 (2003)
 - [66] A. Cebrecos, V. Romero-Garcia, R. Pico, I. Perez-Arjona, V. Espinosa, V. J. Sanchez-Morcillo, and K. Staliunas, Formation of collimated sound beams by three-dimensional sonic crystals, *J. Appl. Phys.* **111**(10), 104910 (2012)
 - [67] E. Schonbrun, T. Yamashita, W. Park, and C. Summers, Negative-index imaging by an index-matched photonic crystal slab, *Phys. Rev. B* **73**(19), 195117 (2006)
 - [68] A. E. Siegman, Defining, measuring, and optimizing laser beam quality, *Proc. SPIE* **1868**, 2–12 (1993)
 - [69] E. O’Neill, Spatial filtering in optics, *IEEE Trans. Inform. Theory* **2**(2), 56–65 (1956)
 - [70] D. Schurig and D. R. Smith, Spatial filtering using media with indefinite permittivity and permeability tensors, *Appl. Phys. Lett.* **82**(14), 2215 (2003)
 - [71] R. Rabaday and I. Avrutsky, Experimental characterization of simultaneous spatial and spectral filtering by an optical resonant filter., *Opt. Lett.* **29**(6), 605–607 (2004)
 - [72] A. Sentenac and A.-L. Fehrembach, Angular tolerant resonant grating filters under oblique incidence, *J. Opt. Soc. Am. A Opt. Image Sci. Vis.* **22**(3), 475–480 (2005)
 - [73] L. Dettwiller and P. Chavel, Optical spatial frequency filtering using interferences, *Journal of the Optical Society of America A* **1**(1), 18 (1984)
 - [74] O. F. Siddiqui and G. V. Eleftheriades, Resonant modes in continuous metallic grids over ground and related spatial-filtering applications, *J. Appl. Phys.* **99**(8), 083102 (2006)
 - [75] Y. J. Lee, J. Yeo, R. Mittra, and W. S. Park, Application of electromagnetic bandgap (EBG) superstrates with controllable defects for a class of patch antennas as spatial angular filters, *IEEE Trans. Antennas Propagat.* **53**(1), 224–235 (2005)
 - [76] Z. Luo, Z. Tang, Y. Xiang, H. Luo, and S. Wen, Polarization-independent low-pass spatial filters based on one-dimensional photonic crystals containing negative-index materials, *Applied Physics B* **94**(4), 641–646 (2009)
 - [77] P. Usik, A. Serebryannikov, and E. Ozbay, Spatial and spatial-frequency filtering using one-dimensional graded-index lattices with defects, *Opt. Commun.* **282**(23), 4490–4496 (2009)
 - [78] R. Pico, V. Sanchez-Morcillo, I. Perez-Arjona, and K. Staliunas, Spatial filtering of sound beams by sonic crystals, *Applied Acoustics* **73**(4), 302–306 (2012)

-
- [79] R. Pico, I. Perez-Arjona, V. Sanchez-Morcillo, and K. Staliunas, Evidences of spatial (angular) filtering of sound beams by sonic crystals, *Applied Acoustics* **74**(7), 945–948 (2013)
- [80] L. Maigyte, T. Gertus, M. Peckus, J. Trull, C. Cojocar, V. Sirutkaitis, and K. Staliunas, Signatures of light-beam spatial filtering in a three-dimensional photonic crystal, *Phys. Rev. A* **82**(4), 043819 (2010)
- [81] J. Trull, L. Maigyte, V. Mizeikis, M. Malinauskas, S. Juodkazis, C. Cojocar, M. Rutkauskas, M. Peckus, V. Sirutkaitis, and K. Staliunas, Formation of collimated beams behind the woodpile photonic crystal, *Phys. Rev. A* **84**(3), 033812 (2011)
- [82] R. Dai, S. Chen, Z. Ren, Z. Wang, and D. Liu, Defect modes in silver-doped photonic crystals made by holography using dichromated gelatin, *Applied Physics B* **109**(1), 15–18 (2012)
- [83] B. J. Chang and C. D. Leonard, Dichromated gelatin for the fabrication of holographic optical elements, *Appl. Opt.* **18**(14), 2407–2417 (1979)
- [84] V. G. Veselago, The electrodynamics of substances with simultaneously negative values of ϵ and μ , *Soviet Physics Uspekhi* **10**(4), 509–514 (1968)
- [85] Y. Cheng, M. Peckus, S. Kicas, J. Trull, C. Cojocar, R. Vilaseca, R. Drazdys, and K. Staliunas, Beam focusing in reflection from flat chirped mirrors, *Phys. Rev. A* **87**(4), 045802 (2013)
- [86] Y. C. Cheng, J. Redondo, and K. Staliunas, Beam focusing in reflections from flat subwavelength diffraction gratings, *Phys. Rev. A* **89**(3), 033814 (2014)
- [87] B. P. Cumming, A. Jesacher, M. J. Booth, T. Wilson, and M. Gu, Adaptive aberration compensation for three-dimensional micro-fabrication of photonic crystals in lithium niobate, *Opt. Express* **19**(10), 9419–9425 (2011)
- [88] B. P. Cumming, S. Debbarma, B. Luther-Davis, and M. Gu, Simultaneous compensation for aberration and axial elongation in three-dimensional laser nanofabrication by a high numerical-aperture objective, *Opt. Express* **21**(16), 19135 (2013)

Trumpos žinios apie autorių

Vardas	Vytautas
Pavardė	Purlys
Gimimo data	1985 09 04
Gimimo vieta	Vilnius
Tautybė	Lietuvis
El. paštas	vytautas.purlys@ff.vu.lt

Išsilavinimas

1996–2004	Vilniaus jėzuitų gimnazija.
2004–2008	Vilniaus universitetas, Fizikos fakultetas. Bakalauras.
2008–2010	Vilniaus universitetas, Fizikos fakultetas. Magistras.
2010–2014	Vilniaus universitetas, Fizikos fakultetas, Kvantinės elektronikos katedra. Doktorantūros studijos.

Mokslinio darbo patirtis

2005–2010	Laborantas, Vilniaus universiteto lazerinių tyrimų centras.
2010–2014	Jaunesnysis mokslo darbuotojas, Vilniaus universiteto lazerinių tyrimų centras.

Mokslinės stažuotės

2007.09–2008.03	Hanoverio lazerinių tyrimų centras, Vokietija
2009.08–2009.09	Šizuokos universitetas, Japonija
2010.09–2011.01	FORTH IESL institutas, Graikija
2010.12.13–17	ES metamedžiagų mokykla „Metamorphose vi“, Graikija
2011.09–2011.12	FORTH IESL, Greece
2012.09.21–22	ES metamedžiagų mokykla „Metamorphose vi“, Rusija
2013.02–2013.04	Šizuokos universitetas, Japonija

Kita

Aukštųjų mokyklų studentų mokslinių darbų premijos laureatas už darbą „Naujų hibridinių fotopolimerų tyrimas ir taikymas trimačių mikrodarinių formavimui“
 Aukščiausi įkopti Čimtarga (5489 m), Monblanas (4810 m), Ak-Baital perėja (4655 m, dviračiu), Fudžijama (3776 m), Kita-dakė (3193 m), Psiloritis (2456 m).

CURRICULUM VITAE

Name **Vytautas**
Last name **Purlys**
Date of birth 1985 09 04
Place of birth Vilnius
Nationality Lithuanian
Email vytautas.purlys@ff.vu.lt

Education

1996–2004 Vilnius Jesuit Gymnasium.
2004–2008 Vilnius University, Faculty of Physics. Bachelor degree.
2008–2010 Vilnius University, Faculty of Physics. Master degree.
2010–2014 Vilnius University, Faculty of Physics, Department of Quantum Electronics. PhD studies.

Professional experience

2005–2010 Laboratory assistant, Vilnius University
Laser Research Center.
2010–2014 Junior research fellow, Vilnius University
Laser Research Center.

Scientific internships

2007.09–2008.03 Laser Zentrum Hannover, Germany
2009.08–2009.09 Shizuoka University, Japan
2010.09–2011.01 FORTH IESL, Greece
2010.12.13–17 EU metamaterials school “Metamorphose vi”, Greece
2011.09–2011.12 FORTH IESL, Greece
2012.09.21–22 EU metamaterials school “Metamorphose vi”, Russia
2013.02–2013.04 Shizuoka University, Japan

Other

Lithuanian Academy of Sciences reward for the work „Characterization of novel hybrid photopolymers and their application for three-dimensional microstructure fabrication“

Highest climbed mountains Chintarga (5489 m), Mont Blanc (4810 m), Ak-Baital pass (4655 m, by bicycle), Fujiyama (3776 m), Kita-dake (3193 m), Psiloritis (2456 m).